Spring 2024

Simulation of Wave Propagation in Granular Particles Using a Discrete Element Model

Syed Tahmid Hussan

SIMULATION OF WAVE PROPAGATION IN GRANULAR PARTICLES USING A DISCRETE ELEMENT MODEL

by

SYEDTAHMID HUSSAN

(Under the Direction of Professor Xiaoming Yang)

ABSTRACT

The understanding of Bender Element mechanism and utilization of Particle Flow Code (PFC) to simulate the seismic wave behavior is important to test the dynamic behavior of soil particles. Both discrete and finite element methods can be used to simulate wave behavior. However, Discrete Element Method (DEM) is mostly suitable, as the micro scaled soil particle cannot be fully considered as continuous specimen like a piece of rod or aluminum. Recently DEM has been widely used to study mechanical properties of soils at particle level considering the particles as balls. This study represents a comparative analysis of Voigt and Best Fit theorem with DEM simulation. Multiple disk shaped uniformly distributed particles are arranged in a square shaped box. This particles are vibrated with a BE that generates shear and compressive wave within boundary area. Wave velocity is then recorded based on the movement of the particles at specific locations. Both S and P wave velocity is monitored based on the contact stiffness for both triangular and square arrangement. The study summarizes that DEM can accurately simulate the wave behavior. Also it shows that first peak method is a promising way to measure wave velocity. However, deviation between theoretical and simulation result occurs due to assuming non uniform stress and discrete element media.

INDEX WORDS: Bender Element, Discrete Element Method, Numerical Model, Granular Material, Wave Velocity

SIMULATION OF WAVE PROPAGATION IN GRANULAR PARTICLES USING A DISCRETE ELEMENT MODEL

by

SYEDTAHMID HUSSAN

B.Sc., Chittagong University of Engineering & Technology, Bangladesh, 2019

M.Sc., Georgia Southern University, USA, 2024

A Thesis Submitted to the Graduate Faculty of Georgia Southern University

in Partial Fulfillment of the Requirements for the Degree

MASTER OF SCIENCE

SIMULATION OF WAVE PROPAGATION IN GRANULAR PARTICLES USING A DISCRETE ELEMENT MODEL

by

SYEDTAHMID HUSSAN

Major Professor: Xiaoming Yang

Committee: Junan Shen

Soonkie Nam

Electronic Version Approved:

May 2024

DEDICATION

To my beloved parents, favorite teachers and all other professors whose unconditional love and support have brought me to present position.

ACKNOWLEDGMENTS

I would like to express my sincere gratitude to my advisor, Dr. Xiaoming Yang. His unwavering support throughout my research journey is invaluable. Dr. Yang's encouragement provided the courage I needed to persevere through all the experiments and analyses. I would also like to extend my appreciation to Dr. Junan Shen and Dr. Soonkie Nam, whose guidance made my coursework clear and manageable. Finally, I am grateful to my parents; without their love and support, I would not be where I am today.

TABLE OF CONTENTS

LIST OF TABLES

LIST OF FIGURES

CHAPTER 1
INTRODUCTION

1.1 Background

Earth crust is subjected to frequent movement due to various natural and man-made reasons. For instance, earthquakes are one of the main natural phenomena responsible for disastrous ground fluctuation. Besides, non-destructive testing, structures impact loading in structures, mining operations, explosive demolition and geothermal energy extraction are some significant human driven means of ground vibration. In the case of natural phenomena, seismological techniques is applied to monitor seismic activity and predict potential ground movements. This information is mobilized for seismic hazards and informing the design and construction of resilient infrastructure in earthquake-prone regions. Human activities can also generate significant ground vibrations that pose risks to nearby structures, ecosystems, and communities. This may involve the use of vibration monitoring equipment to assess the magnitude and propagation of vibrations, as well as the implementation of engineering controls such as damping systems or vibration isolators to reduce the transmission of vibrations to surrounding structures.

.Any sudden movement releases built-up energy that radiates towards surface as seismic waves. This wave is categorized into two major types; S wave causes the particles to vibrate side to side and P wave travel with compression and expansion similar to sound as shown in Figure 1.1. P wave is the fastest seismic waves and travel through solid rock, liquid, and gas while S waves travel slower and only propagate through solid material. Another type of wave named surface wave is also significant. These waves travel along the Earth's surface and are responsible for the most destructive shaking during an earthquake. Surface waves include Love waves and Rayleigh waves, which cause the ground to move in a rolling or shaking motion.

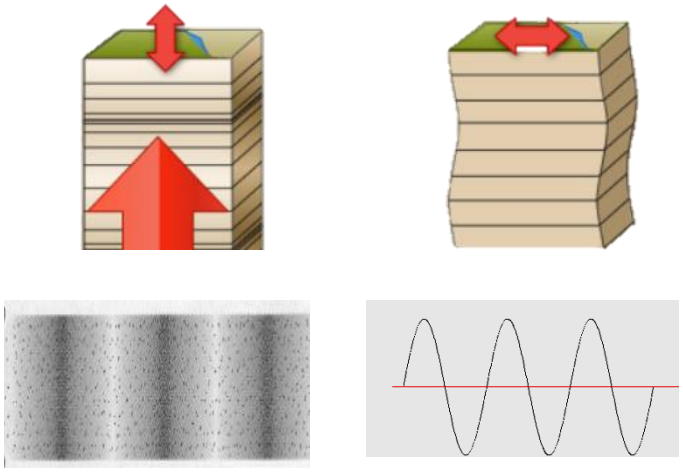

(a) (b)

Figure 1.1 (a) P wave (b) S wave

Measuring seismic wave velocity is important for various applications. It enables accurate seismic hazard assessments by providing insights into how seismic energy propagates through the Earth's crust, aiding in the prediction of earthquake impacts on infrastructure and communities. Additionally, seismic wave velocity measurements are fundamental to earthquake early warning systems, facilitating rapid detection and alerting of impending seismic events, thus allowing for timely emergency response and mitigation efforts. In geological exploration, these measurements help characterize subsurface structures and identify valuable natural resources such as oil, gas, and minerals.

The velocity can be measured both in the field and in simulation. Field measurements involves seismic surveys using specialized equipment and techniques. Seismographs are deployed at various locations to record the arrival times of seismic waves generated by controlled sources such as explosives or vibrators. In recent years, Bender Element (BE) has become popular to measure wave velocities in soils. Standard piezoelectric transducer shows some drawbacks such as poor coupling with particles, unaligned impedance and uncontrolled frequency. Shirley and Hampton (1978) first come over those problems by introducing BE to soil tests. It is now widely used in

laboratory to measure small-strain shear modulus G_{max} and hence, the velocities of waves. Shear wave velocity is a basic mechanical property that has a great importance to understand the interactions between geomaterials at the time of any kind of dynamic loading specially earthquakes and artificial vibrations.

On the other hand, simulation techniques refers to computational models that replicate the behavior of seismic waves in the subsurface. These simulations utilize mathematical equations based on wave propagation theory, considering factors such as the geological properties of the materials through which the waves travel, the source of seismic energy, and the recording instruments' characteristics.This can be done by defining subsurface model, including layer thicknesses, densities, and elastic properties. They then input parameters such as the seismic source type, frequency, and location. The simulation calculates the expected arrival times and waveforms of P and S waves at receiver locations based on the defined parameters and the properties of the simulated subsurface. Using same technic, it is possible to simulate bender element test. One of the renowned method of simulation is Discrete Element Method (DEM). This is a numerical technique used to simulate the behavior of systems composed of discrete elements, such as soil particles, rocks, or grains.

The Particle Flow Code (PFC) developed by Itasca is a widely used software package based on the DEM simulation. PFC has been applied in various fields, including geotechnical engineering, mining, rock mechanics, and soil dynamics, to address practical engineering problems such as slope stability analysis, tunneling, excavation, and soil-structure interaction. This thesis studied particle behavior with different microscopic properties using DEM simulation in PFC. A detailed purpose of this study is described in ‘Objective’ section.

1.2 Objective

This research aims to utilize the Discrete Element Method (DEM) to simulate the propagation of seismic waves (S-waves and P-waves) in granular materials. The specific objectives are:

- Develop and validate a DEM model in PFC to simulate a bender element test using a 1 cm wall as the transmitter and 1 cm diameter balls as particles. The model will be validated for square packing (10,000 balls) and triangular packing (11,413 balls) within a 1 m x 1 m area.
- Investigate the efficiency of the first arrival method for identifying the travel times of S-waves and P-waves using a first peak detection approach on five receivers positioned at specific distances from the bender element.
- Evaluate the influence of contact properties (shear and compressive contact stiffness) on the propagation velocities of S-waves and P-waves within the DEM model.
- Demonstrate the capability of DEM to accurately simulate seismic wave propagation in granular materials and compare the obtained wave velocities with theoretical models (Voigt) and the best-fit hypothesis.
- Compare the DEM results for Poisson's ratio and yield strength with the predictions from the Voigt model and the best-fit hypothesis.
- Analyze the deviations observed between the DEM simulation results for wave velocities, Poisson's ratio, and yield strength compared to the predictions from the best-fit hypothesis and Voigt model. Discuss these deviations in the context of limitations inherent to the DEM approach for simulating granular materials.

1.3 Organization

This study comprises of 5 chapters. The first chapter starts with the introduction that explains a detailed background of the work, provide a comprehensive overview of the wave theories and simulation approach. Chapter 2 provides past research for discrete Element Method (DEM) for granular materials, elastic wave theory, contact property effects on wave speed, typical material properties, existing research on wave speed-property links, and other numerical methods for wave propagation in granular media. The methodology chapter details our approach. We define the simulation space, particle properties, and arrangement method (e.g., square and tringular packing). We then configure the wave transmitter and receiver elements, specifying their size, position, and material properties. Finally, we explain the overall simulation process, including wave generation techniques. Chapter 4 and 5 explore results and analysis for wave reflection within the granular medium and detail how we measured wave travel times to calculate velocities. We analyze how varying contact stiffness affects wave propagation and, compare wave velocities between different packing arrangements. These findings enhance our understanding of wave behavior in granular materials, paving the way for further research on optimizing wave transmission or mitigating reflection effects.

CHAPTER 2
LITERATURE REVIEW

2.1 Concept of Elastic Wave Equation

Elastic waves are a classification of mechanical wave that can propagate through solids causing a temporal deformation of the internal structure. Unlike electromagnetic waves, this can only pass through a medium such as solid, liquid or gas. Particles in the medium can be deformed by compression, shearing or elongation. Elastic waves can propagate in two modes, longitudinal and transverse wave. When a longitudinal wave propagate in a solid medium, the two dimensional wave equation is

$$\frac{\delta^2 s}{\delta t^2} = c^2 \frac{\delta^2 s}{\delta x^2} \tag{1}$$

Here, displacement s, time t, propagation velocity c, $\frac{\delta^2 s}{\delta t^2}$ represents how forcefully the displacement get changed and $\frac{\delta^2 s}{\delta x^2}$ represents how the displacement is being altered in one axis from point x. Derivation of (1) from Hook's Law yields velocity for compressional wave, V_p as, (Articolo 2009)

$$V_p = \sqrt{\frac{E(1-\mu)}{\rho(1+\mu)(1-2\mu)}} \tag{2}$$

Here, Young's modulus *E*, Poison's ration μ and bulk density ρ. If shear modulus is denoted as *G*, then shear wave velocity, V_s

$$V_S = \sqrt{\frac{G}{\rho}} = \sqrt{\frac{E}{2\rho(1+\mu)}} \tag{3}$$

Wave velocity calculated from DEM can be used to determine macroscopic elastic properties by rearranging and combining (2) and (3) as follows-

$$\mu = \frac{2-\left(\frac{V_p}{V_s}\right)^2}{2\left[1-\left(\frac{V_p}{V_s}\right)^2\right]} \quad (4)$$

$$E = \frac{\rho\left(V_p\right)^2(1+\mu)(1-2\mu)}{1-\mu} \quad (5)$$

And from equation (3), shear modulus G can be written as

$$G = \rho V_s^2 \quad (6)$$

2.2 Typical Values of Poison's Ratio and G

The Poisson's ratio and shear modulus are fundamental mechanical properties that describe the behavior of soil under stress. Poisson's ratio, denoted by ν, represents the ratio of transverse strain to axial strain when a material is stretched or compressed. In soil mechanics, Poisson's ratio indicates how much a material will contract laterally when subjected to axial loading. It typically ranges between 0.1 and 0.5 for most soils, implying that soil tends to expand laterally when compressed. On the other hand, the shear modulus, denoted by G, measures a material's resistance to shear deformation. It quantifies the stiffness of the soil in response to shear stress, reflecting its ability to withstand shearing forces without undergoing excessive deformation. Both Poisson's ratio and shear modulus are crucial parameters in geotechnical engineering, influencing the stability and behavior of soil structures such as embankments, foundations, and retaining walls. A typical chart for different values of poison's ratio and G is given in Table 2.1.

Table 2.1 Typical Values of Poison's Ratio and Shear Modulus (Pennington et al. 2001)

Soil type	Description	Poisson's Ratio	G(MPa)
Clay	Soft	0.35-0.4	0.4-5
Clay	Medium	0.3-0.35	5-11
Sand	Stiff	0.2-0.3	11-38
Sand	Loose	0.15-0.25	4-8
Sand	Medium	0.25-0.3	8-16
Sand	Dense	0.25-0.35	16-32

2.3 Effect of Contact Properties on Wave Velocity in Granular Materials

Strain and stress represent foundational concepts essential for comprehending the deformation of solid materials when subjected to external forces. Soild properties such as elasticity and strength characterize the correlation between stress and strain and seismic wave velocity. However, granular media exhibits distinct behavior compared to solid material. Stress strain relationship in granular particles typically nonlinear and governed by particle size, packing density, particle size and other factors. Thus, granular media is more challenging to predict due to its complex nature. Liao et al. 1997 developed a relationship among stress strain behavior with wave velocity and contact properties.

The relation is developed based on two hypothesis. 'Vigot hypothesis' consider only homogenous strain over the particles and 'Best fit hypothesis' consider both mean displacement and uniform strain (Liao et al. 1997). Consider an isotropic packing structure containing rigid particles of same size and material properties and discontinuities in inter-particle contacts, then equations for Young modulus Y, Bulk modulus B, and Poison ration μ are as follows (Liao et al. 1997)-

Based on Voigt hypothesis-

$$E = \frac{4Nr^2K_n}{V}\left[\frac{K_n+K_s}{3K_n+K_s}\right] \quad (7)$$

$$\mu = \frac{K_n-K_s}{3K_n+K_s} \quad (8)$$

$$B = \frac{Nr^2K_n}{V} \quad (9)$$

Based on Best Fit hypothesis

$$E = \frac{8Nr^2K_n}{V}\left[\frac{K_s}{K_n+3K_s}\right] \quad (10)$$

$$\mu = \frac{K_n-K_s}{K_n+3K_s} \quad (11)$$

$$B = \frac{Nr^2K_n}{V} \quad (12)$$

2.4 Prior Research on Wave Velocity Relation with Contact Properties

Wave velocity is dependent upon several micro and macroscale properties of particles such as, gravity, damping ratio, friction coefficient and other contact properties. One of the important contact properties is contact stiffness, responsible for influencing wave velocity, is crucial to assess earthquake hazards and design structures that can better withstand dynamic forces. This relation is defined as micro-macro relationship by Rojek, Madan, and Nosewicz (2019). The author investigated S and P wave behavior with respect to normal and shear contact stiffness ration for ununiformed discs. Many authors observed wave propagation characteristics for different inter particle properties. For example, Sadd, Tai, and Shukla (1993) studied wave attenuation of granular particles with respect to contact contact laws, focusing on granular microstructures. O'Donovan, O'Sullivan, and Marketos 2012 used DEM to compared laboratory results. A cubic

sell with particular material properties was used for the model to assess wave velocities in relation to contact stiffness. In this study, the relation of shear wave velocity in macroscale with normal and shear contact stiffness for uniformly shaped disc like particles is monitored. Simulation result is then compared with Voigt and Best Fit hypothesis derived by Liao et al. (1997).

2.5 Common Signal Interpretation Technics

A lot of controversy still exists to differentiate and measure the velocities of S and P waves. They follow separate paths in different particle layers. For a rectangular shaped sample, P wave travels through two sides and S wave travels to the front as shown in Figure 2.1 (Lee and Santamarina 2005).

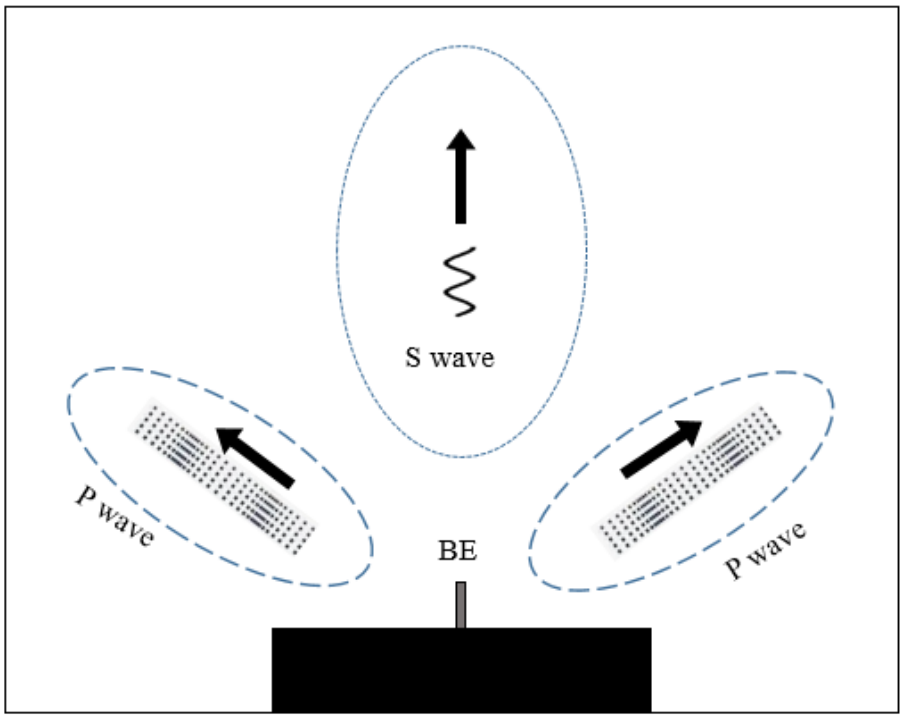

Figure 2.1 S and P wave travel direction for laboratory BE test setup (Lee and Santamarina 2005)

BE signal interpretation is comparatively simple and straightforward. However, accurate measurement of wave travel time is still a challenging task. A wide range of procedures have been

studied to interpret the signal, varying from simplest process related to instantaneous lookup of the signal to enumerate time interval, to more complicated methods such as Fourier decomposition and Spectrum analysis. Authors also suggested diverse wave shapes and configuration based on output transparency and handy interpretation, for instance, Square signal (Dyvik and Madshus 1985), sine wave (Viggiani and Atkinson 1995), sine sweep frequency (Ferreira, da Fonseca, and Santos 2007), sine pulse with 90° phase shift (Pennington, Nash, and Lings 2001) , distorted sine wave with 30° phase shift (Jovičić, Coop, and Simić 1996), forced oscillation at resonant frequency and impulse signal (Lee and Santamarina 2005).

Most early research applied square waves. However, sine wave pulse produced from BE has more accurate time interpretation (Blewett, Blewett, and Woodward 2000). Another great controversy comes out while determining the first arrival peak on output signal. A typical output wave is presented in Figure 2.2 where a single sine pulse has taken as input signal. Then the question arise what is the hit point to the particle; w, x, y or z?

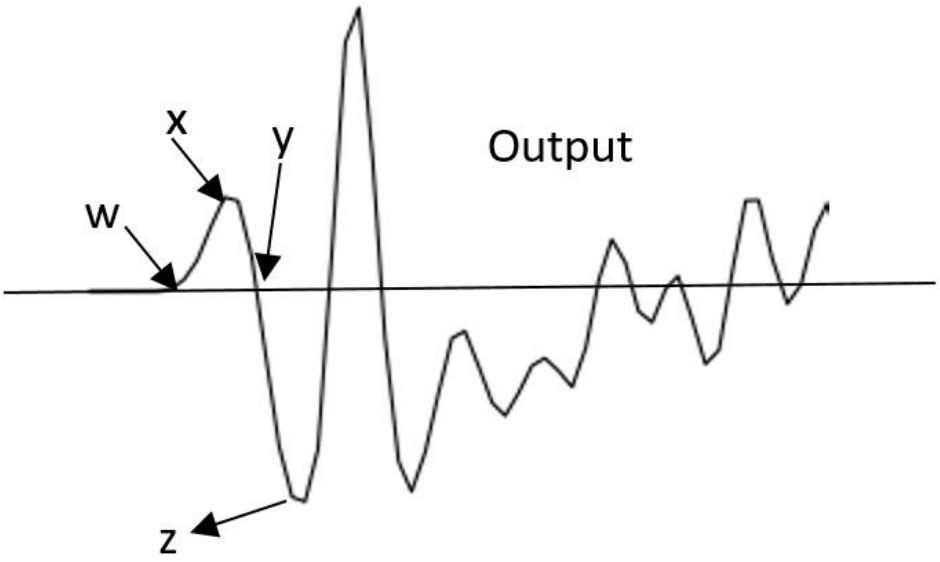

Figure 2.2 Output S Wave in BE: (w) First Deflection, (x) First Peak, (y) Zero after First Peak, (z) Second Peak

The pattern of signal is not always same as shown in above figure. However, a few initial deflection or peaks remain same for most of the received signals. Suggested conditions and criteria differ based on surrounding condition, particle properties, installation of the system and input signal (Jovičić, Coop, and Simić (1996); Dyvik and Madshus (1985); Blewett, Blewett, and Woodward (2000); Lee and Santamarina (2005); Viggiani and Atkinson (1995); Kawaguchi, Shibuya, and Mitachi (2001). Authors also suggested number of technical requirements to receive undisturbed first arrival by avoiding wave interference at sidewall, transducer resonance, grounding and electrical noise. Those requirements include uninterrupted electric connection, noise free environment, rigid transducer base and proper grounding.

2.6 S and P Wave Velocity in Different Granular Media

The velocities of seismic waves in granular media exhibit significant variation depending on the material properties. Studies have shown that denser and stiffer granular assemblies generally transmit waves faster. For example, research by Evangelou et al. (2023) found that S-wave velocities in dry sand can range from 150 m/s to 400 m/s, while P-wave velocities can reach up to 600 m/s. In contrast, looser materials with lower packing densities tend to have slower wave propagation. Abuawad, Miller, and Muraleetharan (2023) reported P-wave velocities as low as 50 m/s in very loose granular materials. These variations highlight the importance of considering the specific granular media properties when interpreting seismic wave behavior. A list of velocities for different soils is listed in Table 2.2.

Table 2.2 Seismic Wave Velocity in Ddifferent Soils (Abuawad, Miller, and Muraleetharan 2023)

Soil Type	Description	S-Wave Velocity (m/s)	P-Wave Velocity (m/s)
Dry Sand (Loose)	Low density, poorly packed	150 - 400	200 - 600
Dry Sand (Dense)	High density, well-packed	400 - 800	800 - 1400
Saturated Sand	Sand filled with water	400 - 600	1500 - 1800
Silt	Fine-grained soil particles	200 - 400	400 - 800
Clay (Soft)	Clay with high water content	100 - 200	200 - 500
Clay (Stiff)	Clay with low water content	200 - 400	400 - 1200
Till	Dense mixture of sand, silt, and clay	400 - 800	800 - 1800
Rock (Soft)	Weakly consolidated rock	800 - 1500	2000 - 4000
Rock (Hard)	Strong and consolidated rock	1500 - 3000	4000 - 6000

2.7 Working Principle of Bender Element

A bender element is a form specialized transducer primarily employed for evaluating shear wave velocity in soils and various granular substances. The transducer is a modified piezo-electric discs, when embedded within the material, induce shear waves upon application of an electrical voltage. BEs have a good soil-transducer interface and a suitable operating frequency, making them practical shear wave transducers for soil molecules. It is a non-destructive test method and convenient for any kind of soil particles to perform in laboratory. In present years, it has become popular in geotechnical engineering as a prompt, low cost and non-destructive process of measuring the stiffness of soil particles.

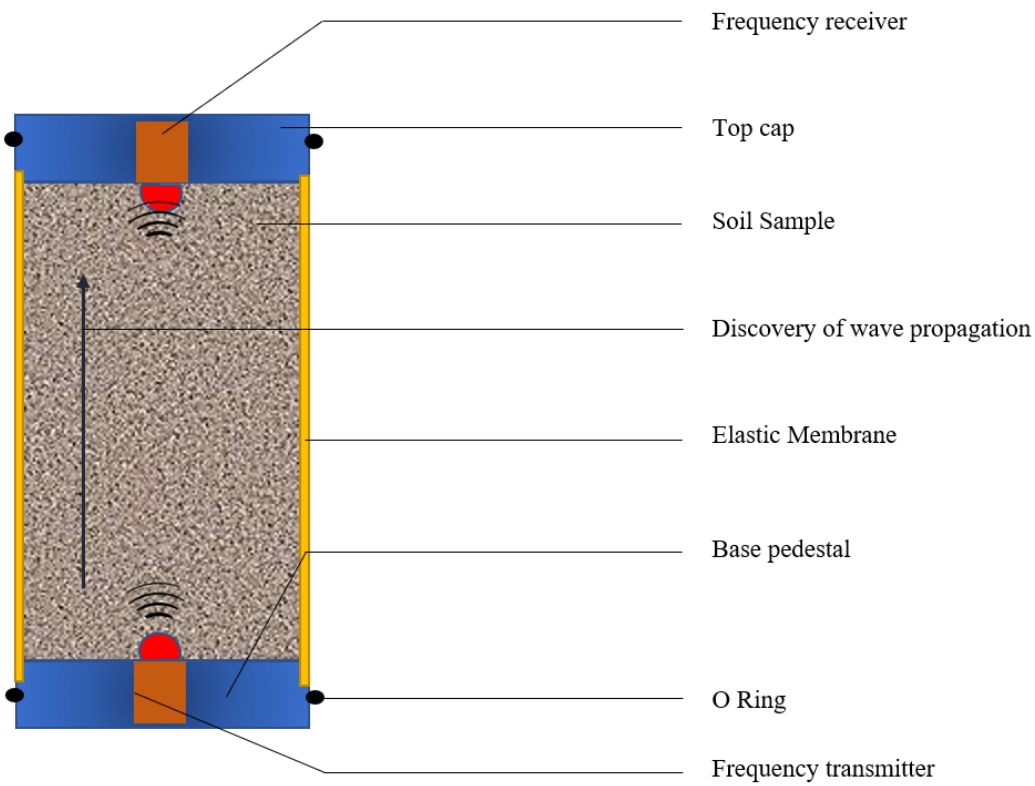

Figure 2.3 Bender Element Setup Mounted on Triaxial Cell

BE comprises of two transducers, transmitter BE receives voltage from the electrical source and converts it into ultrasound vibration. This vibration passes through the particles and later detected by receiver BE. The instrument is set up on a triaxial apparatus with the specimen inside as shown in Figure 2.3. Both vertical and horizontal arrangements are possible. This research simulates the aparatus mounted in the top platen and base pedestal of a triaxial test module as described in the figure above to measure shear wave velocity in the vertical direction. With another bender element positioned on counter directions of a triaxial specimen, an identical method can be used to measure horizontal shear wave velocity. Function generator is used to produce and control signals in the transmitter. Digital oscilloscope connected to a computer is used to capture data. It has two input channels for each of the BE suit. Both a resolution of 2 microseconds and amplitude of 12 mV for

receiver BE. Measured values from consecutive shear wave is averaged to diminish random noise components from the transmitter. Instrument has the averaging function itself in the oscilloscope. Power amplifier is adjusted before connecting to the data recorder.

A preparatory function test is performed through sending a series of square wave to both BEs while placing close to ear to listen a slight clicking sound. Shear wave travel distance is measured between tip to tip point of BE inside the soil specimen. Length of each BE merge into the soil sample that is neglected and subtracted from the height of the sample. The BE transmitter and receiver is kept parallel to function properly and without any buckling effects. Time detected in data receiver is presented with similar polarity. A small time delay (1 mS) may be detected in Bes. This delay is measured by holding two BEs together with slight pressure and no test specimen between them.

2.8 Numerical Methods in Granular Media

Continuum-based numerical methods are being used for years to study the behavior of granular materials, providing valuable information for both qualitative understanding and quantitative analysis. One of the most useful tools is Finite Element (FE) Method, mainly applicable for continuous particles. It can also be used for granular particles considering the limitations. Granular particles like soil are a combination of numerous discontinuous substances. On the other hand, FE is continuous in nature, thus it is complicated to accurately simulate the behavior. The quality and accuracy of a FE model depends on relevant assumption and require complex constitutive models that can simulate the discontinuous behavior. It takes dozens of parameters and computational variables that make the result more accurate but also consume more time steps and become computationally extensive (Mahmood and Elektorowicz 2016). Due to mechanical loading,

environmental conditions and geological processes, soil can undergo micro fractures and bifurcations. In addition, changes in moisture content and temperature induce swelling and shrinking of soil particles, creating internal stresses that can weaken the soil structure through micro fracturing (Figure 2.4). Addressing such deviations necessitates incremental analysis with non-linear elasto-plastic models.

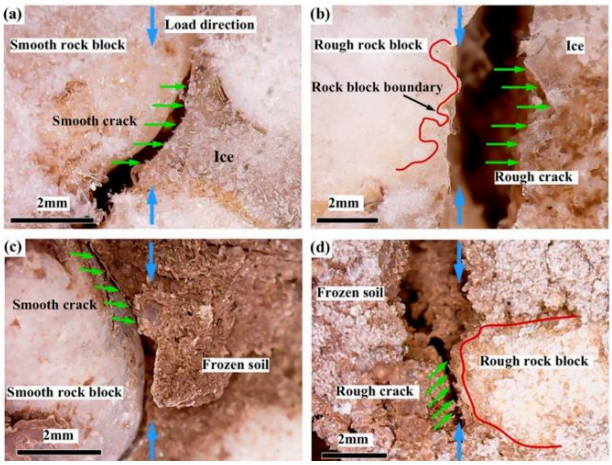

Figure 2.4 Soil-Rock Internal Fractures and Bifurcation (Hu et al. 2021)

2.8.1 Discrete Element Method

To solve the difficulties in simulating granular particles with finite element, researchers developed Discrete Element Method as a discontinuous platform. Unlike continuum-based system, each particle is expressed explicitly, considering individual inter-particle forces and displacement independently. This is first introduced by Cundall (1971) and later applied to soils by P. A. Cundall and Strack (1979). Since then, it's been used by many researchers in the field of geotechnical engineering. Thornton (2000) amongst many others studied inter particle properties with DEM and showed the effects of micro-mechanical response where each particle is assigned specific properties such as contact forces, friction coefficient, size and shape. After completion of the simulation, DEM provides a transparent insights for particle and contact arrangement, flow

characteristics, velocity profile and forces acting on individual particles(Rojek, Madan, and Nosewicz 2019). In geomechanics, quasi static and dynamic analyses is possible by DEM in both bonded and unbonded soil particles (Mouraille, Herbst, and Luding 2009). DEM is also a competent platform to apply in the field of roadways and asphalt engineering (Meegoda and Chang 1993). All of this research indicates DEM a powerful tool to examine the microscale characteristics of granular system and evaluate their behavior under specific loading and boundary conditions. The base of DEM depends on Newton's second law of motion and force displacement law. These are applied on each of the particles and their contacts respectively. Individual particle subjected to a force (can be an external force or gravity) results in motion which is determined by Newton's law and contact forces are calculated with force-displacement law(P. A. Cundall and Strack 1979). Initially, a group of discrete particles with specific size and shape is considered in a bounded area. An imaginary 2D or 3D coordinate system represents the positions. Preliminary data such as gravity, particle density, contact stiffness, friction coefficient and other necessary inputs are specified. Based on those parameters, contact detection module identifies which pair of particles are interacting and force is applied accordingly.

After setting all the preliminary parameters, setting up appropriate timestep is most important to balance computational efficiency and accuracy. An optimum timestep depends on particle acceleration, velocity and characteristic timescale of the system dynamics. An large timestep lead to inaccurate particle interaction and result in system instability while too small timestep can significantly incur computational costs without necessarily enhancing accuracy.

Velocities and displacements for individual particle are calculated by integrating the equation of motion and recorded incrementally in each timestep. The equation of motion can be written as (Mahmood and Elektorowicz 2016)

$$m_i \frac{dv_i}{dt} = \sum_{j=1}^{n} F_{xij} + m_i g \quad (13)$$

And angular velocity is

$$I_i \frac{d\omega_i}{dt} = \sum_{j=1}^{n} L_{xij} \quad (14)$$

Where,

I_i = Inertia of body i

ω_i = Angular velocity of body i

m_i = Mass of body i

v_i = Velocity of body I

n = Total number of particles

F_{xij} = Inter-particle force between body i and j

g = gravity

2.8.2 PFC and Distinct Element Method

Particle Flow Code (PFC) is the geotechnical simulation software introduced by Itasca in 1996. It uses the principle of Distinct Element Method which is slightly different from Discrete Element because of the limitation to be restricted to rigid bodies only ("PFC — PFC 6.0 Documentation,"). rigid bodies refer to solid objects or entities that do not deform under applied forces. These are typically used to represent solid structures, boundaries, or fixtures within a simulation. Unlike particles, which can experience deformation and displacement, rigid bodies maintain their shape and position throughout the simulation. They are employed to model walls, floors, boundaries, supports, or other structures that interact with the granular or discontinuous materials being simulated. They contribute to the overall realism and accuracy of simulations by providing a means to represent solid objects and their interactions with the surrounding materials. Wall, blocks, ball

and clumps are four types of rigid bodies used in PFC. Newton's second law and displacement law is applicable to the rigid bodies except the wall where Newton's second law is not applicable as motion is applied by the user. Rigid body interaction is a dynamic process and it becomes equilibrium if the internal forces get balanced. Individual particle tracking is possible in PFC where contact force, displacement, velocity, acceleration and stress are traced in each timestep. Speed of propagation in this this dynamic process is contingent upon the physical characteristics of the discontinuous particles.

PFC is developed based on seven assumption- rigid particles, article shape is a disk (2D) and sphere (3D), set of pebbles act as clump, internal force and moment act on contact between a pair of bodies, overlap is applicable at soft contact, particles have bonds in contacts and energy potential function is applied to calculate long range interactions ("PFC — PFC 6.0 Documentation,").

2.8.3 Simulation Workflow of PFC

The process of conducting a simulation in PFC involves several key steps. It begins with defining the model geometry and assigning properties to particles and bodies. Boundary conditions and material properties are then specified, followed by the definition of interactions between particles and other entities. Simulation parameters are configured, including timestep size and duration. Initialization of the simulation involves setting initial conditions for particle motion. The simulation is then executed, and results are monitored and analyzed to gain insights into system behavior. Post-processing tasks involve visualization and data extraction for further analysis or interpretation. For each of the cycles, timestep is determined at i^{th} cycle and law of motion is applied. The the cycle goes to i+1 and detects the contacts where force displacement law is

analyzed. This process is continued over each of the cycles and can be recorded the data at any level of cycle. A step by step workflow is illustrated in Figure 2.5.

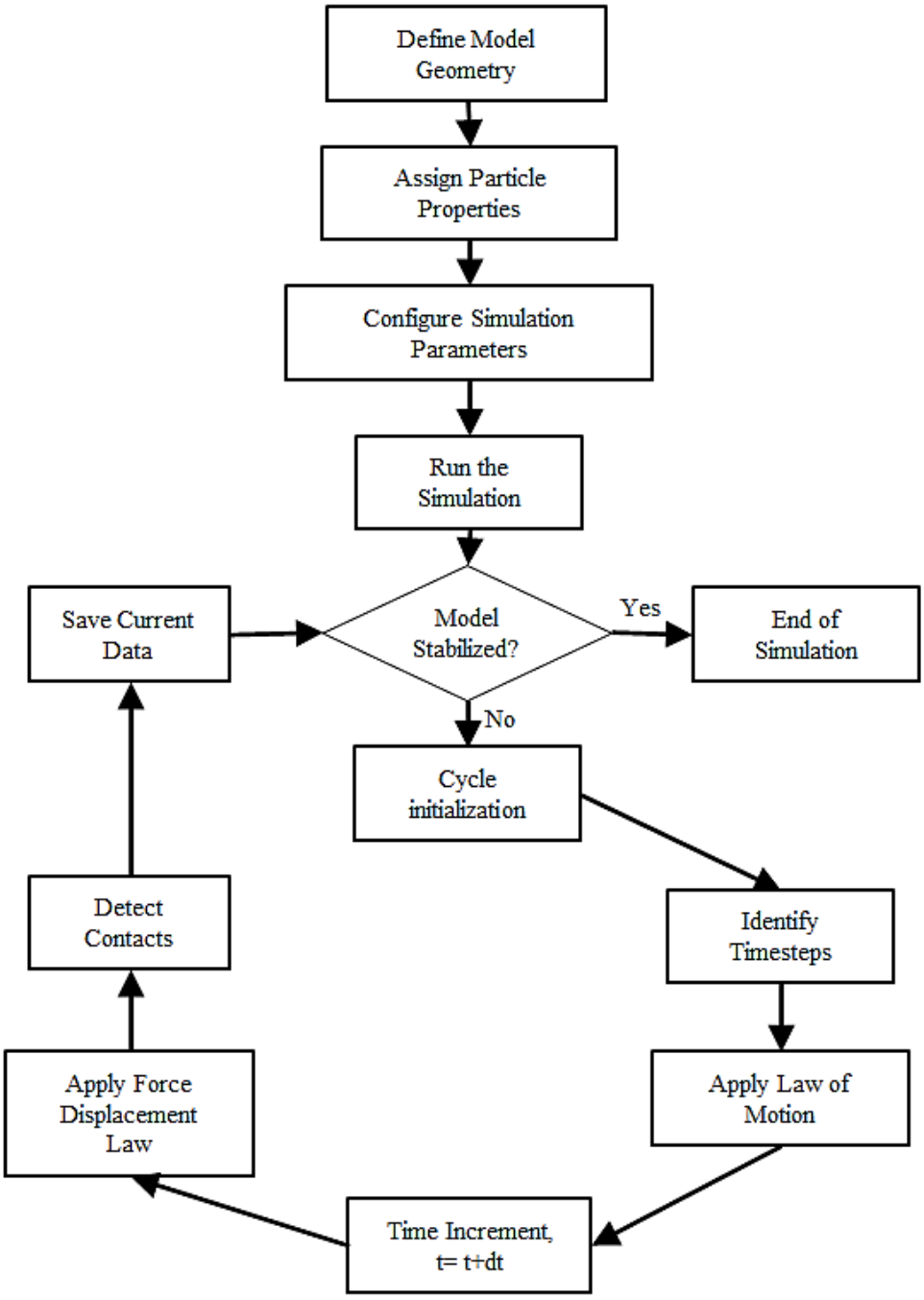

Figure 2.5 PFC Workflow

2.8.4 Contact Models

Contact models considers the forces and displacements that occur at particle-particle and particle-boundary contacts, influencing both micro and macro nature of the simulation. PFC offers various contact models to represent different types of interactions, such as linear elastic, linear viscoelastic, and nonlinear plastic contact models("PFC — PFC 6.0 Documentation,"). Models are classified based on normal and tangential forces, friction and cohesion, allowing for the accurate representation of complex particle behaviors (P. A. Cundall 1988). It is crucial to apply the best constitutional contact model that provides microscopic parameters required to represent the granular behavior on a macroscopic scale.

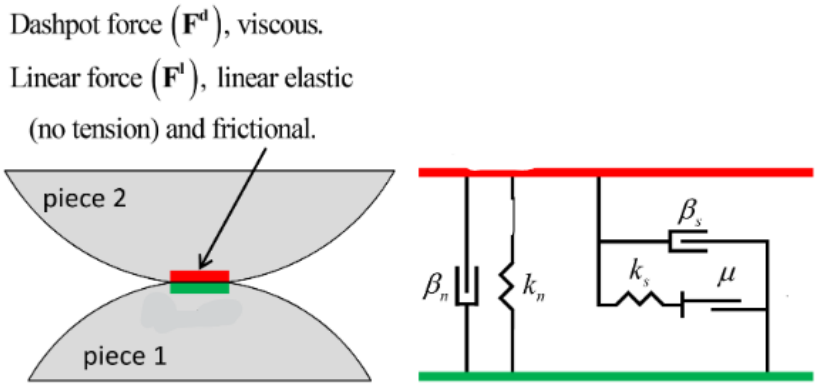

Figure 2.6 Linear Contact model (PFC 6 documentation)

contact models provide a means to accurately capture the complex interactions between individual particles or discrete elements within a material assembly. Among the available options are the Linear and Linear contact bond model, the soft bond model, the Flat joint model, and the Hertz model, each tailored to specific material properties and behavior. For instance, the Linear contact bond model represents a simple yet effective approach to simulating contact between particles,

offering insights into the deformation and failure mechanisms within granular assemblies. In Figure 2.6 of the software documentation, a typical illustration of the liner contact model is presented, showcasing the arrangement and behavior of particles under applied loads.

The linear model with inactive dashpots and a reference gap of zero corresponds with the model of Linear and Linear Contact Bond. This model, integrated within the PFC software, embodies a linear-based approach applicable to both ball-ball and ball-facet contacts. It combines linear and dashpot components operating in parallel to simulate the mechanical behavior of materials. The linear component mimics linear elastic behavior, representing frictional forces without tension, while the dashpot component introduces viscous behavior. Despite their distinct characteristics, both components operate over an infinitesimally small area, transmitting forces without imparting significant deformation.

Several authors also used other contact models. Dong et al. (2018) explores how models like the Hertz Model or Rolling Resistance Linear Model impact the simulated behavior of granular materials under shear compared to the Linear Model. Mas Ivars et al. (2008) reviews various techniques for modeling BPMs, including the use of the Smooth Joint Model and Flat Joint Model for simulating the bonded interfaces. Yin and Yang (2019) investigates rock joint behavior under compression. It utilizes the Hertz Model to capture the non-linear response of the rock during fracture. Rojek et al. (2012) explores different bonding models, potentially including the Adhesive Rolling Resistance Linear Model, to represent the cohesive behavior of granular materials with bonding agents.

CHAPTER 3
METHODOLOGY

3.1 Model Domain and Boundaries

The foundation of simulation lies on predetermining the geometry and setting the domain. PFC requires setting the domain first which is an imaginary boundary area where all the particle interactions and model object is placed. This prevents particles escaping or being stuck in an infinite space, causing numerical instability in the simulation. The command platform along with an interacting graphical plotting board that works in real time while run the code. Plot area illustrates both 3D and 2D. However, this can be performed only in separate PFC GUI designed specifically for 2D or 3D. In this study, 2D module is used with (-6,6) domain extent. Plot has default Cartesian coordinate with origin (0,0) in the middle. Any model object can be settled within the domain based on the imaginary origin.

The particle container, a 0.25 square meter box, encapsulates the simulated particles, ensuring confinement and control over their movement. Each side of the square container is fortified by walls, standard model objects in PFC, providing structural integrity and defining the boundaries of the simulation environment. Notably, the bottom base and top wall are widened by 25 cm on each side from the origin, allowing for ample space for particle interaction. Vertical side walls are strategically positioned at (-0.25, -0.5) and (0.25, +0.5) coordinates, confining particle movement within the defined boundaries.

Importantly, to induce shear wave propagation, a 1 cm Bender Element is precisely situated at the origin (0,0) in a vertical orientation, imparting controlled mechanical stimuli to the particle assembly. Side walls have no mechanical force exerted on them. Only the top part of BE can move freely while bottom remain fixed at (0,0) position. Figure 3.1 illustrates the setup arrangement.

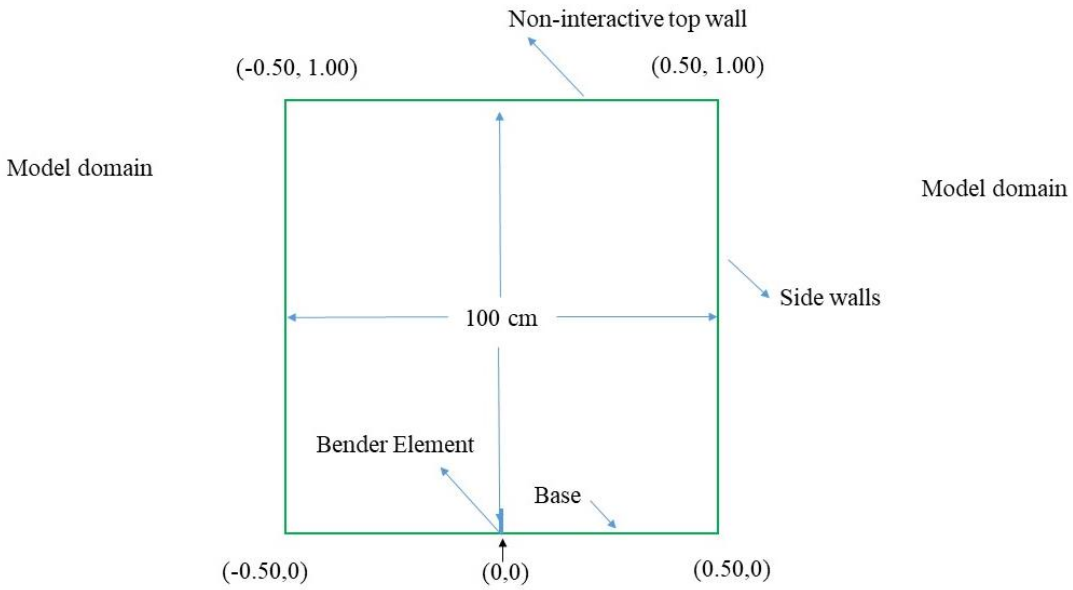

Figure 3.1 Model Domain and boundaries

3.2 Model Properties

In simulations involving particle interactions, mandatory predefined material properties play a pivotal role in establishing contacts and determining necessary forces. Within the simulated domain, Earth's gravitational acceleration of 9.81 m/s^2 is commonly utilized as a uniform gravitational field, ensuring consistency across the particle interaction area. This gravitational force serves as a fundamental parameter for calculating interactions, imparting realism and accuracy to the simulated dynamics.

Monitoring shear wave velocity in relation to normal and shear contact stiffness is crucial for understanding the mechanical behavior of materials under different loading conditions. In this context, six sets of shear contact stiffness are employed, each paired with a single normal contact stiffness where the normal stiffness (kn) exceeds the shear stiffness (ks). Maintaining a consistent ratio between ks and kn ensures systematic exploration of material behavior across various stiffness regimes. By observing how shear wave velocity changes in response to alterations in contact stiffness, it is possible to looks into the material's resistance to deformation and its ability

to transmit shear waves efficiently. The simulation maintains a fixed friction coefficient of 0.65 and a damping ratio of 0.01 throughout the analysis. Consistent frictional behavior and damping characteristics allow for a focused investigation into the effects of varying contact stiffness on shear wave propagation.. Table 3.1 summarizes the properties applied on the model and particles.

Table 3.1 Model Parameters

Symbol	Parameter	Value	Units
n	Number of particles	11343	-
r	Particle radius	.005	m
f	Friction coefficient	.65	-
dr	Damping ratio	.01	-
ρ	Particle density	2400	kg/m^3
V	Particle volume	.0045	m^3
N	Number of contacts	25000	-

Normal contact stiffness K_n (N/m)	Shear contact stiffness, K_s(N/m)
10^6	$3\times10^5, 5\times10^5, 7\times10^5, 9\times10^5, 1\times10^6$
10^7	$3\times10^6, 5\times10^6, 7\times10^6, 9\times10^6, 1\times10^7$
10^8	$3\times10^7, 5\times10^7, 7\times10^7, 9\times10^7, 1\times10^8$

3.3 Particle Arrangement

In the controlled loop applied to position the ball objects within the geometry, a systematic arrangement is maintained to ensure homogeneity and avoid any overlap between the 11 balls. The positioning process involves arranging the balls in rows denoted as n and n+1. For each row,

specific coordinates are assigned to the balls, ensuring a minimum gap between them. Suppose two balls are located at points (a, b) and (c, d) in the n row, with a distance of h between the n and n+1 rows (Figure 3.2). The position of the third ball along the x-axis and at a distance h from the n+1 row is calculated using the Pythagorean theorem, considering the geometric relationship between the points. That means, the subsequent rows are placed in such a way that keep minimum gap between balls and with tangential contacts without any overlap. This systematic approach guarantees a uniform distribution of the balls within the geometry, facilitating accurate simulations and analysis of particle interactions.

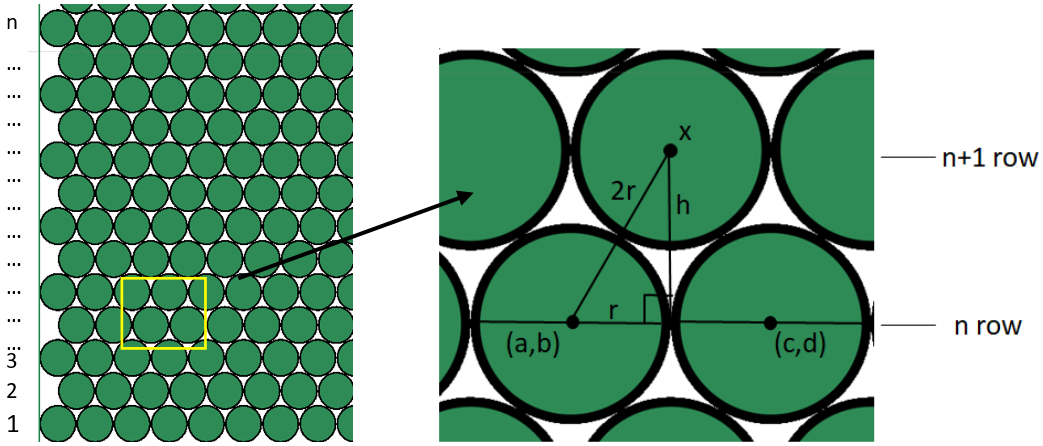

(a)

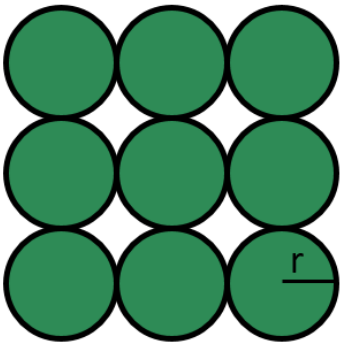

(b)

Figure 3.2 Particle Arrangement in Boundary Area, (a) Triangular Packing (b) Square packing

The mid point of (a,b) and (c,d) is

$$\left(\frac{a+c}{2}, \frac{b+d}{2}\right)$$

Then X coordinate of x is

$$\left(\frac{b+d}{2} + h\right).$$

h is calculated as follows,

$$h = 4r^2 - r^2 = 3r^2$$

Hence

$$x = \left(\frac{a+c}{2}, \frac{b+d+6r^2}{2}\right)$$

In the iterative process of positioning the ball objects within the geometry, the distances h and x are calculated for each row based on the previous row, proceeding systematically through the entire model. By iterating in this manner, a triangular packing arrangement is generated, ensuring that the minimum gap between balls is maintained while avoiding any overlap. This approach enables the creation of a tightly packed configuration where each ball is positioned in a manner that optimizes space utilization and maintains uniformity throughout the model.

3.4 Bender Element Setup

This study aims to emulate the application of Bender Element (BE) technology within a triaxial-type test environment. Typically, in triaxial testing, the BE is mounted between the top platen and the base pedestal of the test specimen. In the simulation model, the horizontal wall object positioned at the bottom represents either the platen or the base pedestal. Function generator is

used to generate and drive signal to the transmitter. The same thing is applied in simulation with a spinning wall positioned vertically on the pedestal.

In the experimental setup, a function generator is employed to generate and drive signals to the transmitter. This process ensures controlled signal input for accurate measurements and analysis. Similarly, in the simulation, a spinning wall is positioned vertically on the pedestal to mimic the function generator and piezoelectric strip's role (Figure 3.3). The spinning wall serves as a virtual counterpart to generate and transmit signals within the simulated environment.

To record simulation output for each timestep, an individual digital storage oscilloscope or an oscilloscope interface connected to a computer is utilized as a data recorder. This is achieved through the PFC command 'history', which captures and stores the simulation data at regular intervals throughout the simulation process. By employing this command, it is possible to effectively monitor and analyze the evolution of system parameters over individual timestep, enabling the detailed examination of dynamic phenomena within the simulated environment. The recorded data is then be further processed and analyzed using Python, Jupyter and Exel, allowing for the extraction of valuable insights into the behavior and performance of the simulated system.

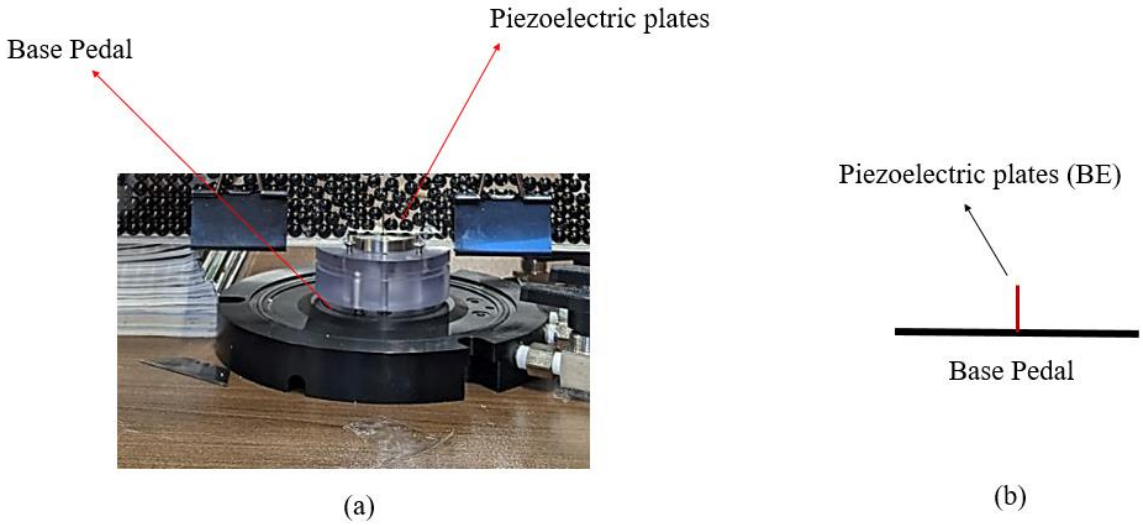

Figure 3.3 (a) Transmitter and Receiver BE in Laboratory, (b) Transmitter BE for Simulation

3.4.1 Receiver Bender Element Setup

In a manner similar to the transmitter, the receiver BEs (Bender Elements) consist of piezoelectric metal plates mounted on a rigid base material. These receiver BEs are strategically positioned within the simulation environment to detect the arrival of waves generated by the transmitter. When a wave reaches the adjacent ball of the receiver, it imparts movement to the ball, causing deformation of the piezoelectric plate and generating a voltage difference across its surfaces. This voltage difference, resulting from the mechanical deformation induced by the wave, is then captured and analyzed by the oscilloscope interface connected to the computer. In the simulation setup, five individual receivers, labeled from B1 to B5, are positioned at specific distances from each other. Each receiver is situated exactly above the transmitter BE and placed vertically to avoid any wave reflection effects from the side walls. The distances between the receivers are as follows: The distance between B1 and B2, B2 and B3, B3 and B4, as well as B4 and B5, is 0.1385 m. However, the distance between B2 and B3 is 0.1212 m, as mentioned in Figure 3.4.

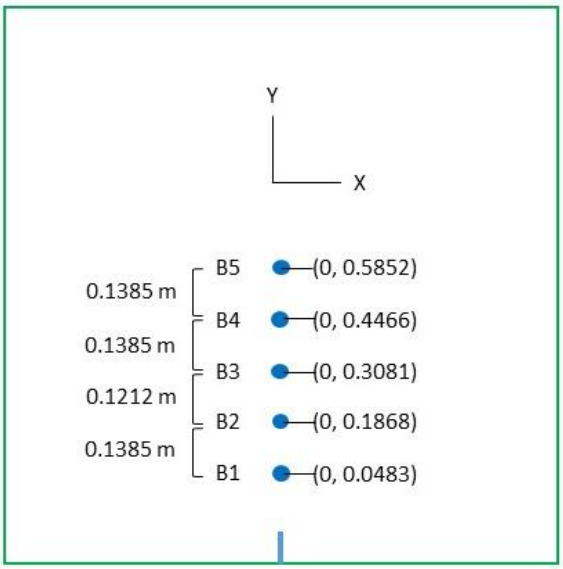

Figure 3.4 Receiver BE in the Simulation

In lieu of installing separate Bender Elements (BEs) at each position, the balls themselves can act as receivers in the simulation setup. Each ball's velocity is monitored individually, serving as a proxy for the received wave at that particular position. Using the 'history' command, the velocity data of each ball is recorded over time, effectively capturing the received wave signals. PFC has comprehensive tools for monitoring various parameters, including velocity magnitude, as well as the x and y components of velocity. Leveraging these capabilities simplifies the process of obtaining both S-wave and P-wave velocities simultaneously within the simulation environment for individual balls.

3.4.2 Wave Generation

In the simulation scenario described, where a 1 cm Bender Element (BE) is utilized, a strain of 0.01% results in a small angular movement of 4 degrees on each side of the BE, totaling an 8-degree movement. This level of strain is analogous to the requirements in laboratory non-destructive testing, where precise control over strain levels is essential to avoid damaging the material under investigation.

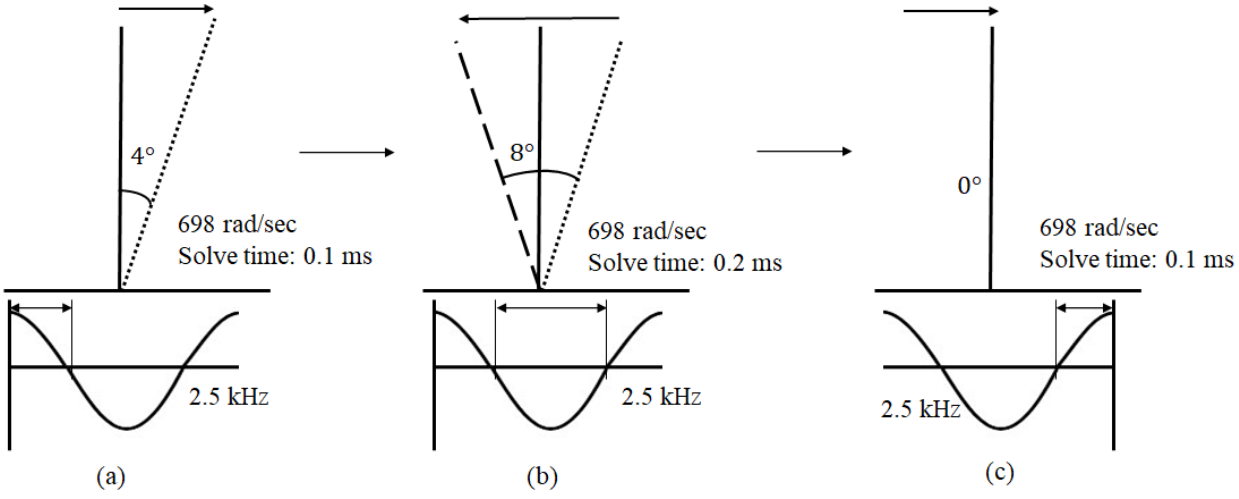

Figure 3.5 Wave Generation in Bender Element

In this PFC simulation, the application of angular velocity on Bender Elements (BEs) is facilitated through two essential wall attributes: "Rotation center" and "Spin." Rotation Center: This attribute sets the fixed point of the BE around which it will rotate. It specify the pivot point for the rotational movement of the BE as illustrated in Figure 3.5. This ensures that the BE rotates around a specific point within the simulation environment, allowing for precise control over its movement. The "Spin" attribute determines the angular velocity of the BE, measured in radians per second. It fixes the rate at which the BE rotates around its rotation center.

Table 3.2 Bender Element Parameters

Symbol	Parameter	Value	Units
h’	BE transmitter height	0.01	m
d’	BE width	.009	m
ω	Rotational velocity	698	rad/sec
	Number of signals	1	-
ϵ	Strain	0.01%	
f’	Frequency	2500	Hz

In this study, the simulation setup utilizes one complete wavelength, achieved through a series of three steps. Initially, the wall is deflected at 698 radians per second for 0.4 milliseconds, leading to a 4-degree inclination from its origin. This action completes 1/4 of the wavelength. Subsequently, the wall is deflected at -698 radians per second, resulting in a clockwise movement of 8 degrees, thus completing 3/4 of the wavelength. Finally, the same angular velocity is applied in the clockwise direction, returning the Bender Element (BE) to its initial position, effectively

completing one full wavelength. After completing one full wavelength and returning to the vertical position, the BE stops. This subtle motion serves as a trigger, generating waves in the surrounding particles. These waves propagate upward through the particle medium, transmitting dynamic forces and displacements as they travel towards the top of the simulation domain. Parameters for BE is listed in Table 3.2.

3.5 Simulation Procedure

Discrete Element Simulation (DEM) in PFC involves several essential steps to accurately model the behavior of granular materials and simulate complex dynamic processes. Initially, the simulation domain is constructed by defining the geometry and properties of the particles, boundaries, and any external forces or constraints. Next, the simulation parameters, including material properties, contact models, and time step settings, are specified to ensure realistic representation of particle interactions. Once the simulation setup is complete, the simulation is executed, with PFC tracking the motion and interactions of individual particles over time. During the simulation, data on particle velocities, forces, displacements, and other relevant variables are recorded at regular intervals using the 'history' command for subsequent analysis. More elaboration is given in the following sections.

3.5.1 Initial Stabilization

Initially, an extent of 36 square meters is designated using ‘model domain’ command to encapsulate the particle interaction area. Boundaries are meticulously configured based on the specifications outlined in section 3.1 of the simulation protocol. Additionally, the Bender Element (BE) is strategically positioned at the coordinate (0,0), serving as a pivotal component within the

simulated environment. Then a loop is executed to position the balls in the correct locations within the boundary.

Following the positioning of the balls, the subsequent step involves defining their density to further refine the simulation setup. This is achieved through the 'ball attribute density' command, wherein a density of 2400 kg/m^3 is set, ensuring that the balls accurately represent the real-world material they simulate. Furthermore, to govern the interactions between particles, the 'Contact cmat default model liner' is implemented, establishing a linear contact model that dictates how particles interact upon contact. Subsequently, a total of 18 simulations are conducted, each varying based on the values of Kn (normal contact stiffness) and Ks (shear contact stiffness) as delineated in Table 3.1. Throughout each simulation case, a friction coefficient of 0.65 and Earth's gravity of 9.81 m/s² are maintained, providing consistent parameters for accurate analysis and comparison of results.

After setting all the properties, 'model solve' command is called to initiate the core simulation process. This command sets the simulation into motion, enabling the system to evolve over time. Notably, this phase of the simulation stops once the model achieves its equilibrium state, draw a balance in the forces and interactions within the simulated environment. The duration of the solving process varies significantly depending on the specific values assigned to Kn and Ks, as these parameters directly influence the dynamics and complexity of the simulated system.

3.5.2 Wave Transmission

During this stage, rotation center, rotational velocity, and solve time are configured in accordance with the specifications outlined in section 3.5. The 'Spin' command is employed to specify the angular velocity with precision, ensuring the accurate representation of dynamic processes. Additionally, 'model solve time' is utilized to set the duration for solving specific step. ‘Spin -698’, ‘model solve time 0.0001’ means the wall rotates at 698 rad/sec anticlockwise for 0.0001 second,

leads to approximately 4 degree inclination. Next, ‘spin 698’ and ‘solve time 0.0002’ specify the wall top rotates at same angular velocity but clockwise direction for 0.0002 sec for almost 8 degree. Lastly, the same procedure applied again in clockwise for 4 degree, results the wall come to initial position (0 degree). These steps complete one wavelength in 0.0004 s resulting 2.5 kHz frequency. The wall becomes standstill at initial position (Figure 3.6). However, wave gradually proceed upward until the model comes to equilibrium or specific timestep met.

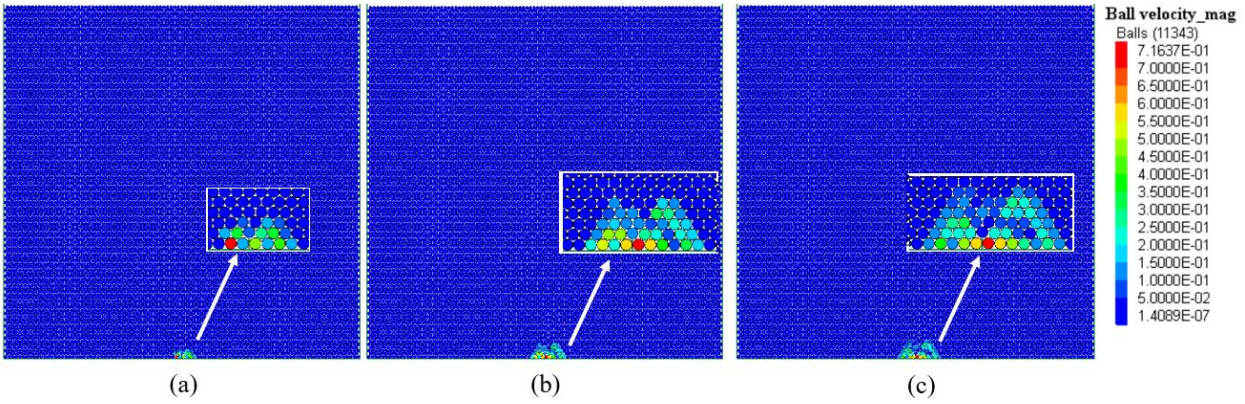

Figure 3.6 (a) Wall Rotation at 0.1 ms, 4° Inclination, (b) Wall Rotation at 0.3 ms, 8° Inclination (c) Wall Rotation at 0.4 ms, 0° Inclination

3.5.3 Data Collection and Analysis

The process of data saving initiates upon the occurrence of the first rotation of the Bender Element. X and Y components of velocity for every individual ball, alongside the mechanical time, are recorded against each timestep. This comprehensive dataset is captured using the 'Ball history' command. Notably, for each set of Kn and Ks values, a distinct group of data is obtained, providing a detailed snapshot of the system's behavior under varying conditions. Subsequently, all collected data is exported to a CSV file, ensuring accessibility and ease of manipulation for further analysis. Exported data is processed Jupyter with Python.

CHAPTER 4
RESULT AND ANALYSIS

4.1 Wave Reflection Effect

The simulation takes place within a 1*1 meter box containing disk-shaped particles. To mitigate the wave reflection effect at the sidewalls, boundary element receivers (BE receivers) are strategically positioned in the middle of the box. This arrangement prevents false identification of the first wave, ensuring accurate analysis of wave propagation dynamics. This phenomenon is illustrated in Figure 4.1, where the spatial distribution of particles and the placement of BE receivers are depicted. Specifically, a group of balls marked 'A' is situated adjacent to the left sidewall. At t=1 ms, these balls exhibit higher velocity compared to their surroundings, indicating the initiation of a wave.

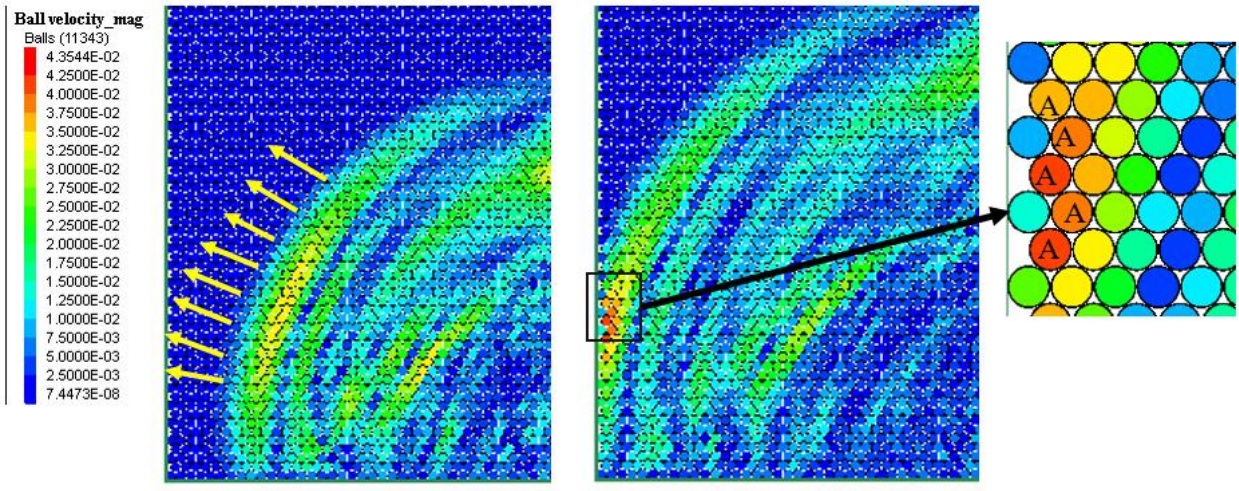

Figure 4.1 Wave Reflection

The X component of one ball within this 'A' region is illustrated in Figure 4.2, revealing distinctive wave characteristics. Notably, the wave exhibits a greater deflection in the middle compared to its front and rear sections, suggesting complex wave behavior during propagation.

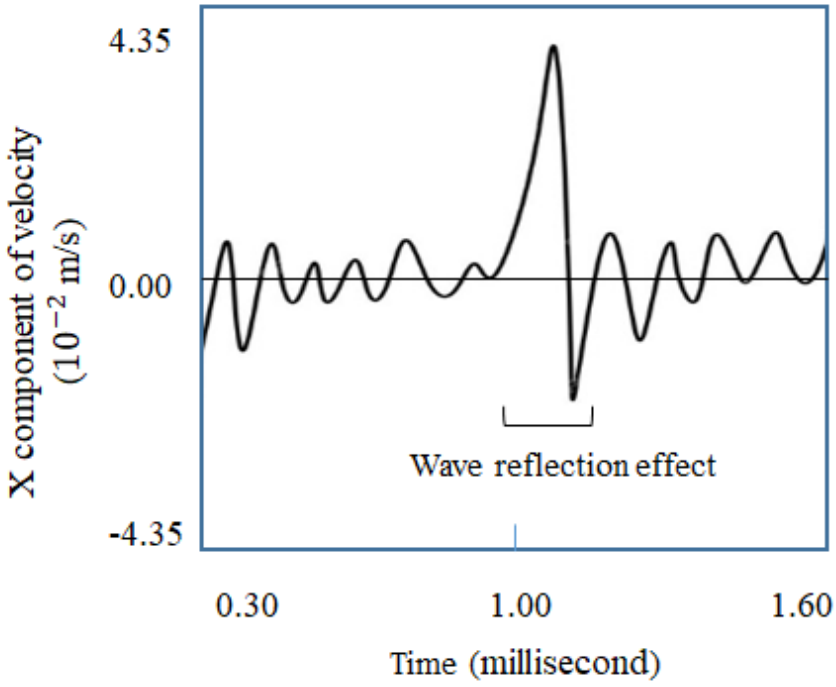

Figure 4.2 Wave Superimposition on Balls Near Sidewall

Figure 4.2 shows that the amplitude of the frequency ranges from -0.01 m/s to 0.01 m/s, observed for 0.30 to 0.80 ms and 1.2 to 1.6 ms. At the time of wave reflection, time 0.90 to 1.1 ms shows the highest peak of around -0.0235 m/s to 0.04 m/s. Amplitude on both side of the reflection peak has almost similar trend. Considering a ball close to the boundary wall leads to the false identification of peak as the value in the reflection zone is higher than both sides. It can mimic the first peak. This incident can lead to interference patterns and false signals that distort the measurement of the ball's exact movement. In particular, waves reflected from the boundaries can superimpose with the original wave, creating complex waveforms that are challenging to interpret. As a result, the precise identification of the ball's position and velocity becomes obscured, introducing errors and uncertainties into the measurement process. Signal received at a ball near boundary may require techniques like signal filtering or advanced data processing algorithms to separate the true ball movement signal from the reflected waves.

4.2 Measurement of Contact Numbers

Contacts represent points where the balls touch each other. These contacts are not pre-defined but are automatically generated and deleted during the simulation process and controlled by linear contact model in PFC. This approach reflects a more realistic scenario where the number of contact points can change as the balls interact and move under the influence of the seismic wave. The study focuses measurement of contacts based on two specific packing geometries: triangular and square packing. These are refer to how balls are arranged in a two-dimensional space. Triangular packing represents a denser arrangement compared to square packing. An important control parameter is that the size of the individual balls remains constant throughout the experiment. This ensures that any observed differences in wave behavior are solely due to the packing arrangement and not the size of the particles.

Table 4.1 Contact Numbers

Serial	Triangular pattern	Square pattern
1	24799	19322
2	25218	19657
3	25160	19791
4	25279	19243
5	25000	19655
6	24871	19754
7	25006	19559
8	24835	19436
9	25043	19740
10	24905	19638

Contact measurement process is divided into two phases. In the initial phase, contacts are established once the material properties, contact model, and external forces such as gravity are applied to the system. This phase allows the system to reach equilibrium, wherein the particles, or balls in this context, settle into a stable configuration under the influence of gravity. Once equilibrium is achieved, BE receivers are activated. At this step, contacts are measured on each timestep as the first wave propagates and strikes specific receiver balls. Average contats 25000 for triangular arrangement and 19500 for square packing is considered. A chart of different contact number received at each specified step is shown in Table 4.1.

4.3 Measurement of Wave Travel Time and Velocity

When the Bender Element reaches equilibrium under gravity, it begins to fluctuate and generate waves. At 0.10 milliseconds, a force initiates movement in a small region of balls (Figure 4.3a). The wave then propagates upwards, hitting ball B1 (Figure 4.3b) and causing it to move in both the x and y directions. The wave continues upwards, striking each subsequent ball. To measure the wave's travel time, the velocities of four balls are tracked. Figure 4.4 shows the x-component of the velocity for the first four balls (B1 to B4). Each gray dot represents the first peak, indicating the ball's x-velocity when the wave first hits. The ball moves back and forth, generating positive and negative displacements that result in opposite velocity signs. Each ball is positioned at a specific distance. The first hitting time is obtained from Figure 4.4 and used with the ball distance to calculate the velocity. Figure 4.5 depicts the relationship between distance and wave travel time, with the tangent indicating the wave velocity. This is just one example for Kn and Ks values of 10 N/m. The same approach is applied for other contact stiffnesses, and the resulting wave velocities are compared for five shear contact stiffnesses against three normal contact stiffnesses.

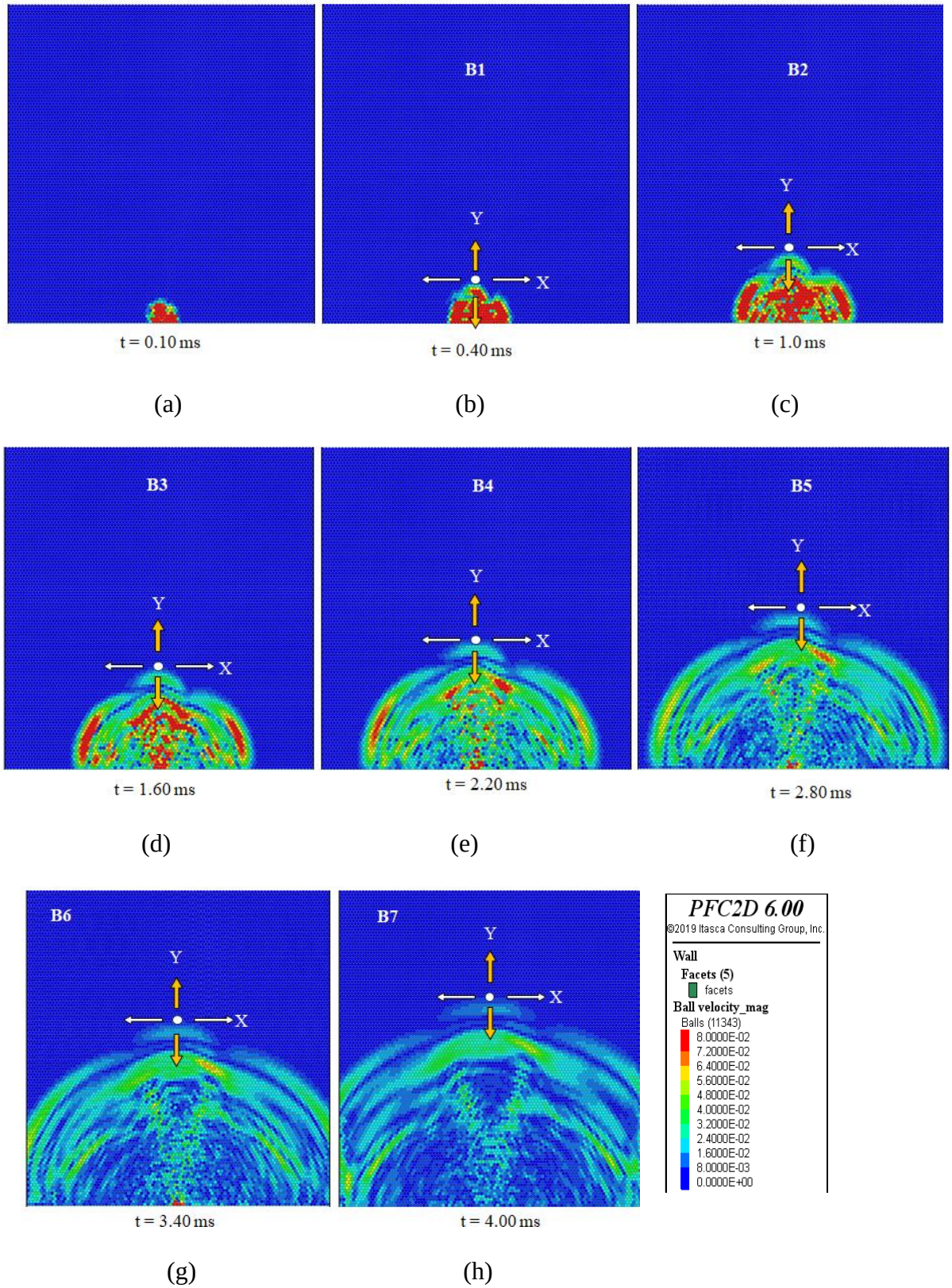

Figure 4.3 Illustration of Simulation Result

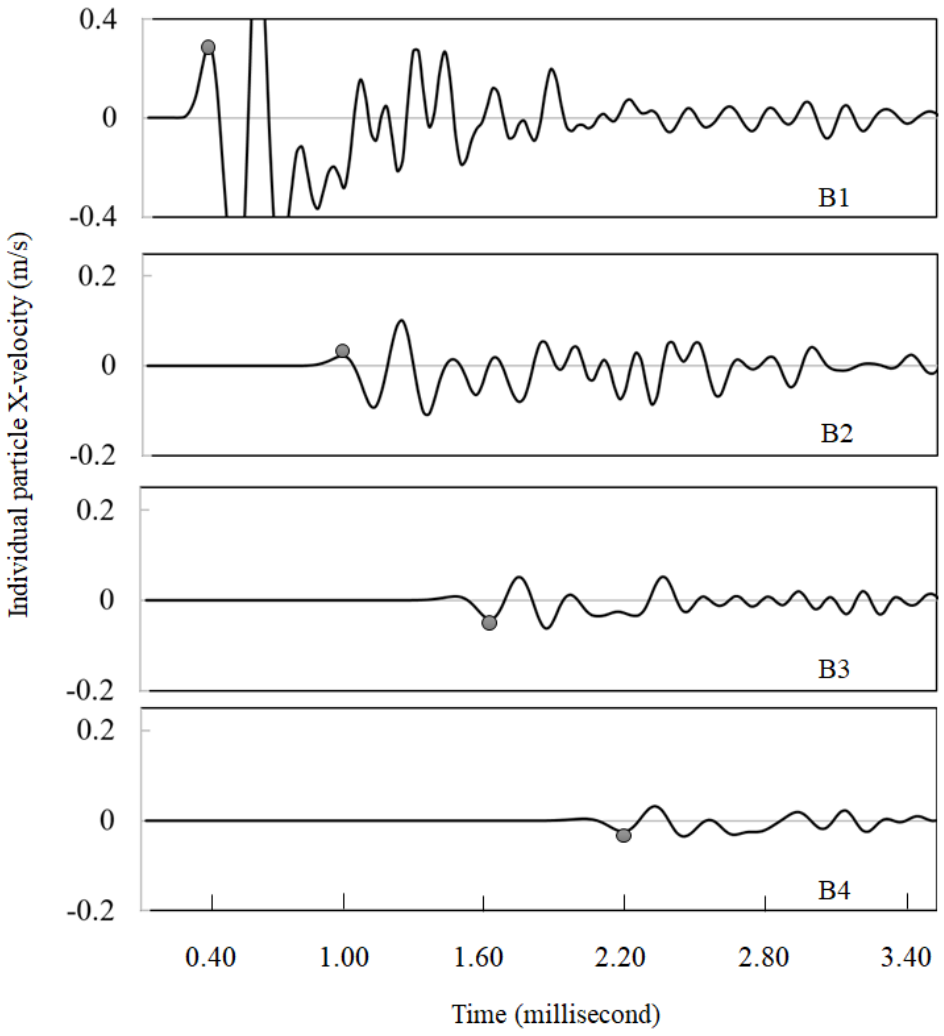

Figure 4.4 Ball Velocity Profile

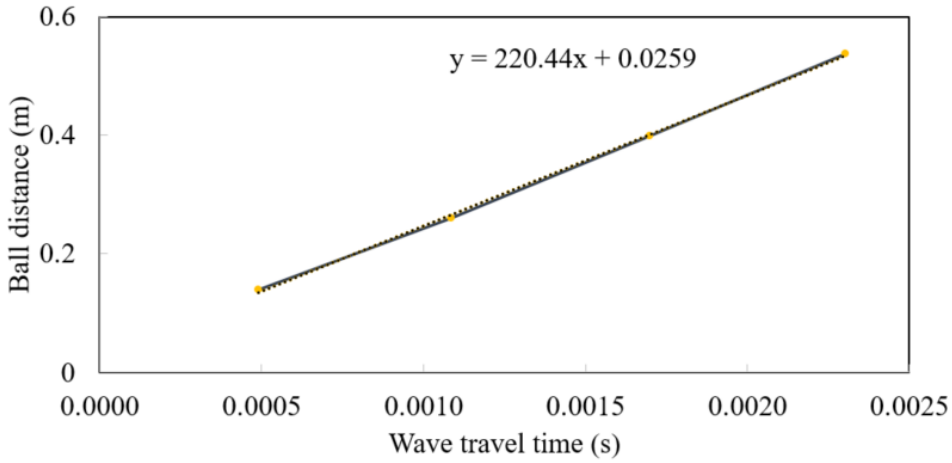

Figure 4.5 Wave Velocity Profile

4.4 Velocity with Contact Stiffness (Triangular Packing)

This section lays the groundwork for deeper insights into the dynamic interplay between contact stiffness and wave propagation. Here, the focus lies on explaining the intricate relationship between wave velocity and contact stiffness within the simulated environment. Each value of Kn comprised of five Ks which is analyzed to ascertain their influence on wave propagation characteristics. The section further discuss the comparison of P-wave and S-wave velocities obtained from both simulation data and theoretical equations. Equation (2) is employed to calculate the P-wave velocity, while equation (3) is utilized for determining the S-wave velocity. Wave velocity measurement technic is described in section 4.4.

The three figures (Figure. 4.6) depict the relationship between wave velocity and contact stiffness (Ks) for two wave types: P-waves and S-waves. However, they are representing Kn of $10^6, 10^7 \text{and } 10^8$ N/m (Figure 4.6 a, b, c) consecutively. The x-axis represents contact stiffness, and the y-axis represents wave velocity. Each graph displays two pair of data sets; P and S wave velocity received from both simulation and equations. The first graph (Figure 4.6 a) shows that simulation P wave velocity is approximately 280 m/s for Ks 3×10^5 N/m which is increased at around 300 m/s at 10^6 N/m. Similarly, simulation S wave velocity is almost 160 m/s for the same Ks which is increased at 210 around m/s at 10^6 N/m.

The same trend is observed for rest of the figures. However, for Kn $10^7 \text{and } 10^8 \text{N/m}$, it can be seen a major jump in wave velocity. In Figure 4.6 (a), the starting velocity is 150 m/s for S wave and 270 m/s for P wave which is amplified to 450 m/s for S wave and 850 m/s for P wave in figure 4.6 c,d. This clearly indicate a proportional upward trend for both type of wave similar to the velocity calculated from the equations. However, calculated velocities for both Voigt and Best Fit are higher than those are enumerated from simulation.

For example, calculated P wave velocity at Ks 10^5 N/m is approximately 20% higher than simulation while calculated S wave velocity at the same Ks is around 28% higher than simulation. The second two graphs (Figure 4.6 c,d) delineates velocity and Ks relation for Kn is 10^7 N/m. Calculated S and P velocity shows a greater jump from Kn 10^6 N/m to 10^7 N/m which is same for simulation result. However, equation derived velocities are also higher than simulation for this case as well. Calculated S wave velocity at Ks 10^7 N/m is approximately 15% higher than simulation, increased from 500 m/s to 750 m/s for Voigt equation and 600 m/s to 750 m/s for Best Fit. However, calculated P wave velocity at the same Ks is around 9.6% higher than simulation (Figure 4.6 c, d).

This clearly indicates a similar trend for both first and second figure. The third row if figure 4.6 depicts the relationship for Kn 10^8 N/m. This time simulation and equation derived results are appearing to be more close than other two Kn. For all the Kn values, S wave velocity is more closer to the result from Best Fit equation. More specifically, it gets close when the Ks value is lower. (Figure 4.6 a, c, e). Compared to the S wave, P wave shows a greater deviation in from equation results. Though the P wave velocity from simulation has a greater difference from equation derived velocity, it gets reduced with the increase of Ks.

On the other hand, S wave velocity shows almost uniform difference for any value of Ks. Most importantly, for both S and P wave at any of Kn values, velocity becomes same when the Ks/Kn ratio is 1. This clearly indicate that wave velocity comparison is more convenient to be figured when displayed against Ks/Kn ratio.

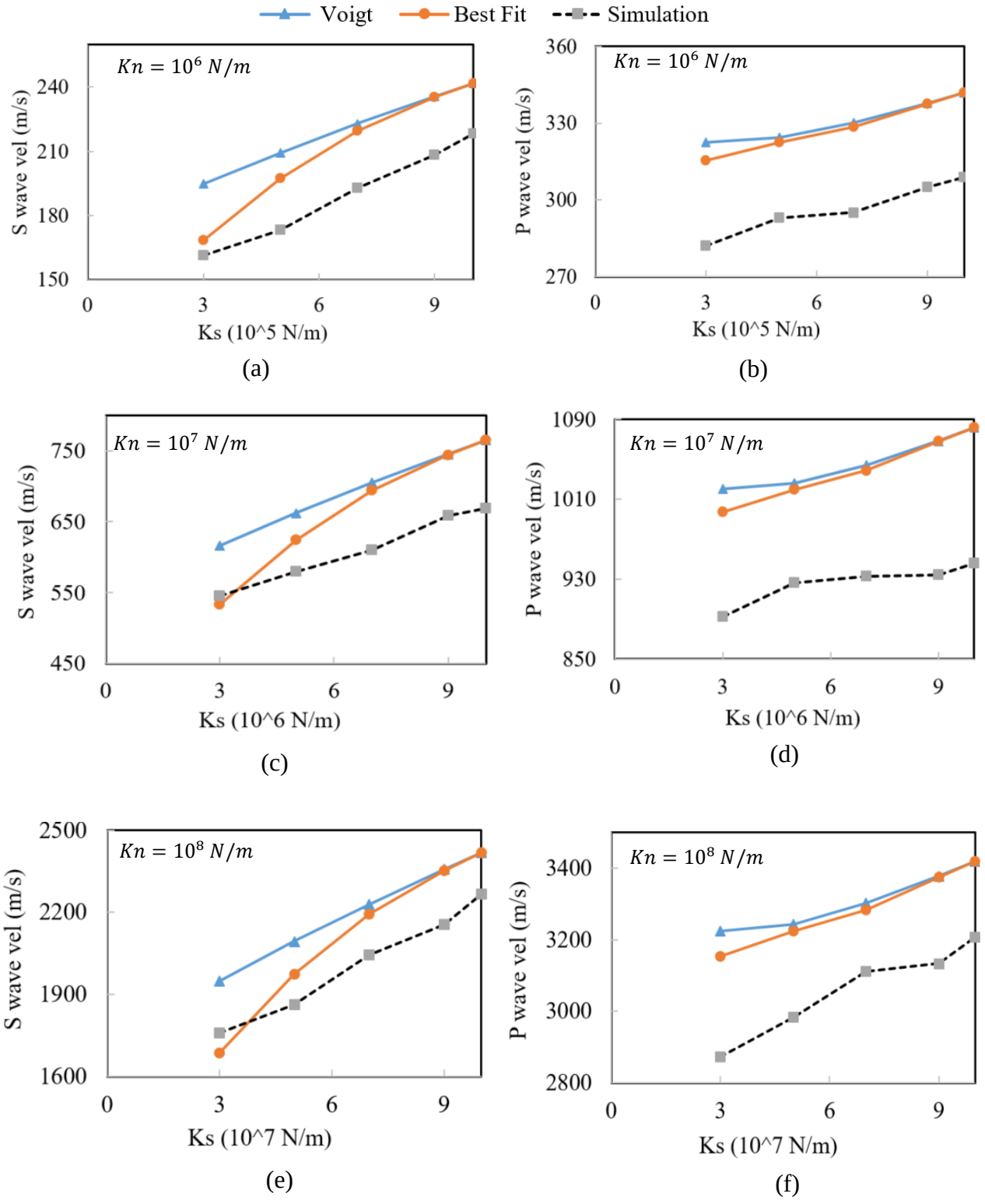

Figure 4.6 Relation Between Contact Stiffness and Wave Velocity for (Triangular Packing)

4.5 Young's Modulus and Poison's Ratio with Contact Stiffness (Triangular Packing)

Both Voigt and Best-Fit equations are derived for Young's modulus and Poisson's ratio. A comparison of these results from the equations and DEM simulations is illustrated in Figure 4.7 and 4.8. To obtain normalized results and a more convenient illustration, the ratio of Young's modulus to the initial Young's modulus is plotted on the Y-axis, and the Ks/Kn ratio is plotted on the X-axis.

Figures 4.7 and 4.8 present results for different Kn values: 10^6 N/m (Figure 4.7a), 10^7 N/m (Figure 4.7b), and 10^8 N/m (Figure 4.7c). The dotted line represents the DEM simulation results, while the black and red lines depict the predictions from Voigt's theory and the Best-Fit equation, respectively. For both Poisson's ratio and Young's modulus, the simulation results generally align well with either the Best-Fit equation or Voigt's theory. In Figure 4.7b (Kn = 10^7 N/m), the simulation result nearly overlaps with the prediction from Voigt's theorem. In contrast, Figure 4.7a (Kn = 10^6 N/m) shows better agreement with the Best-Fit equation. Interestingly, Figure 4.7c (Kn = 10^8 N/m) displays a mixed trend: the simulation result matches Voigt's prediction up to a Ks/Kn ratio of 0.7 and then settles in the middle of both lines.

When considering Poisson's ratio, the simulation results primarily agree with the Best-Fit equation. Figure 4.8a (Kn = 10^6 N/m) shows perfect agreement at a Ks/Kn ratio of 1, with a slight deviation towards higher values as the ratio decreases. Similarly, Figure 4.8b (Kn = 10^7 N/m) exhibits a near-perfect match at a Ks/Kn ratio of approximately 0.27. Overall, these findings suggest that the normalized Poisson's ratio results for the triangular packing pattern exhibit good agreement with the Best-Fit equation. Despite the good agreement observed here, the deviations could be attributed to limitations of the models used, such as the assumptions made about particle interactions or the exclusion of factors like particle imperfections.

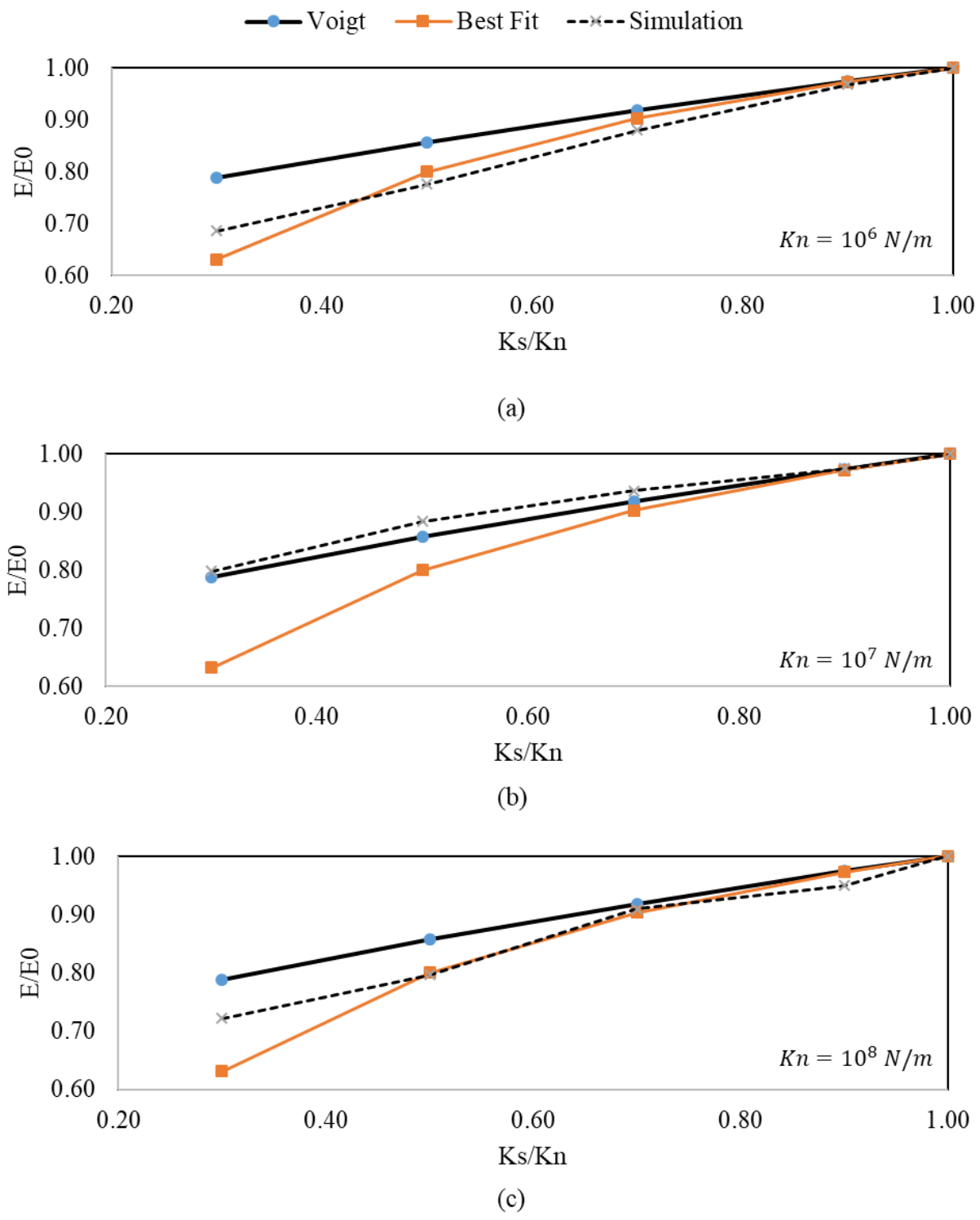

Figure 4.7 Characteristics of Contact Stiffness with Yield Strength (Triangular Packing)

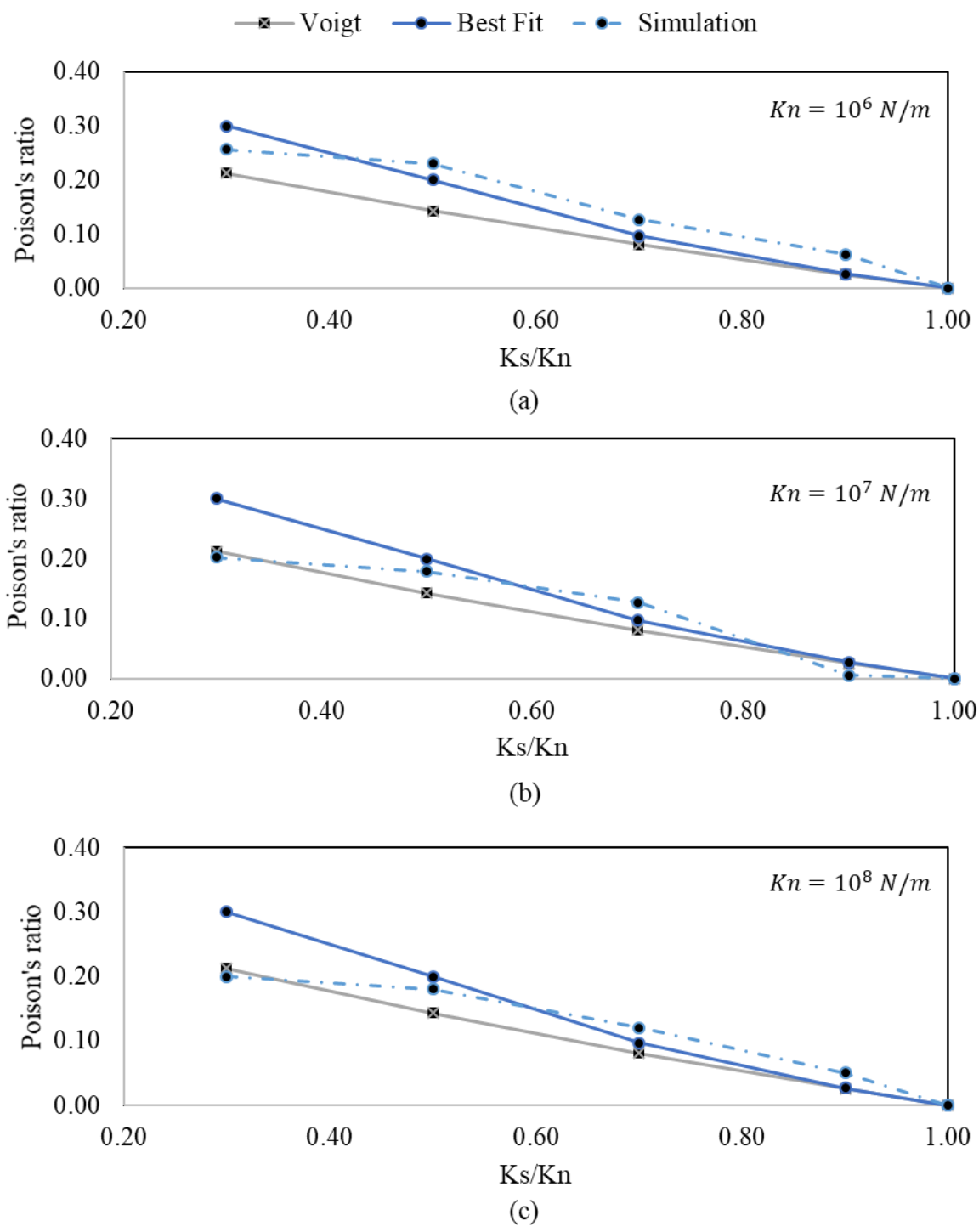

Figure 4.8 Characteristics of Contact Stiffness with Poison's Ratio (Triangular Packing)

4.6 Wave Velocity with Contact Stiffness (Square Packing)

Similar to triangular packing, wave velocities are observed for square packing. The first graph (Figure 4.9 a) shows that simulation P wave velocity is approximately 230 m/s for Ks 3×10^5 N/m which is increased at around 265 m/s at 10^6 N/m. Similarly, simulation S wave velocity (Figure 4.9 b) is almost 150 m/s for the same Ks which is increased at around 180 m/s at 10^6 N/m. Similar trend is seen for rest of the figures.For Kn $10^7$and 10^8N/m, a major jump is observed for wave velocity. In figure 4.9 (a, b), the starting velocity is 150 m/s for S wave and 230 m/s for P wave which is increased to around 450 m/s for S wave and 740 m/s for P wave in figure 4.9 c,d. This clearly indicate a proportional upward trend for both type of wave similar to the velocity calculated from the equations. However, calculated velocities for both Voigt and Best Fit are higher than those are enumerated from simulation in square packing that resembles the triangular pattern.

For example, calculated P wave velocity at Ks 10^6 N/m (Figure 4.9 b) is approximately 16% higher than simulation while calculated S wave (Figure 4.9 a) velocity at the same Ks is around 27% higher than simulation. The second two graphs (Figure 4.6 c,d) delineates velocity and Ks relation for Kn is 10^7 N/m. Calculated S and P velocity shows a greater jump from Kn 10^6 N/m to 10^7 N/m which is same for simulation result. However, equation derived velocities are also higher than simulation for this case as well.

The third row in figure 4.9 one depicts the relationship for Kn 10^8 N/m. This time simulation and equation derived results are appearing to be more close than other two Kn. For all the Kn values, S wave velocity is more closer to the result from Best Fit equation. More specifically, it gets close when the Ks value is lower.

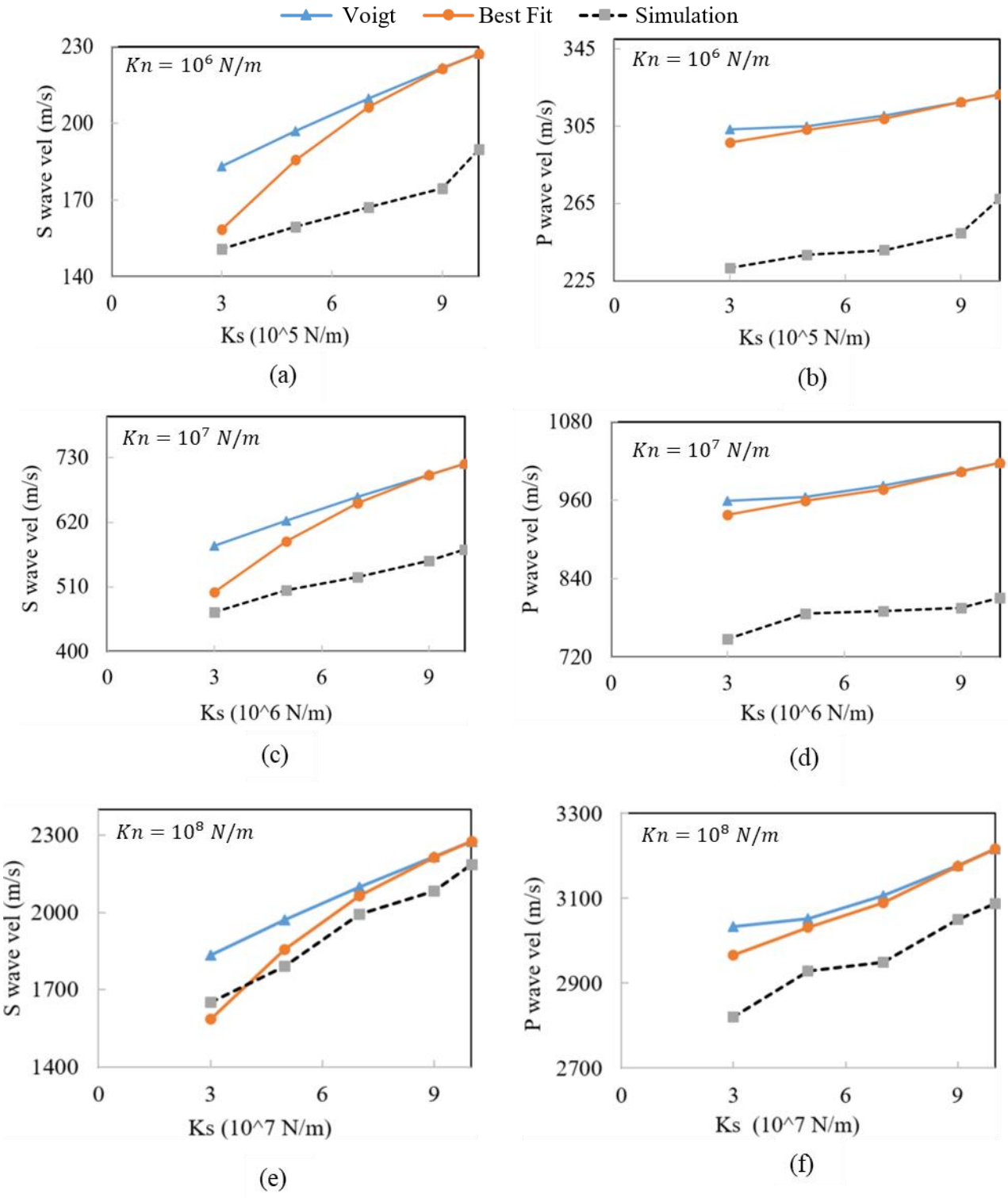

Figure 4.9 Relation Between Contact Stiffness and Wave Velocity for Square Packing

4.7 Young's Modulus and Poison's Ratio with Contact Stiffness (Square Packing)

Similar to triangular packing, Figures 4.10 and 4.11 compare the predictions of Young's modulus and Poisson's ratio from both Voigt and Best-Fit equations with the results obtained from DEM simulations for square packing. To facilitate a clearer comparison, the results are normalized. The Y-axis shows the ratio of Young's modulus to its initial value, while the X-axis presents the Ks/Kn ratio.

Figures 4.10 and 4.11 shows results for different Kn values: 10^6 N/m (Figure 4.10a), 10^7 N/m (Figure 4.10b), and 10^8 N/m (Figure 4.10c). The dotted line indicating the DEM simulation results, while the black and red lines depcits the predictions from Voigt's and the Best-Fit equation results, respectively. For both Poisson's ratio and Young's modulus, the simulation results mostly shows similar trend with either the Best-Fit equation or Voigt's theory. In Figure 4.10b (Kn = 10^7 N/m), the simulation result nearly overlaps with the prediction from Voigt's theorem. In contrast, Figure 4.10a (Kn = 10^6 N/m) does not show a trend similar to any of the solutionsn. However, Figure 4.10c (Kn = 10^8 N/m) displays a mixed trend: the simulation result matches Voigt's prediction up to a Ks/Kn ratio of 0.6 and then settles in the middle of both lines.

When considering Poisson's ratio, the simulation results agree with both Voigt and Best-Fit equation depending on the value of Kn. Figure 4.11a (Kn = 10^6 N/m) shows a lower value of simuation result compared to equations. However, Figure 4.11b (Kn = 10^7 N/m) exhibits a near-perfect match with Voigt theorem while figure 4.11c mathces mostly with Best Fit.

Overall, these findings suggest that the normalized Poisson's ratio results for the square packing shows closeness depending on the value of Kn. Similar to the deviaiton found in tringular pattern, square pattern could alo be attributed to assumptions made about particle interactions or the exclusion of factors like unifrom stress.

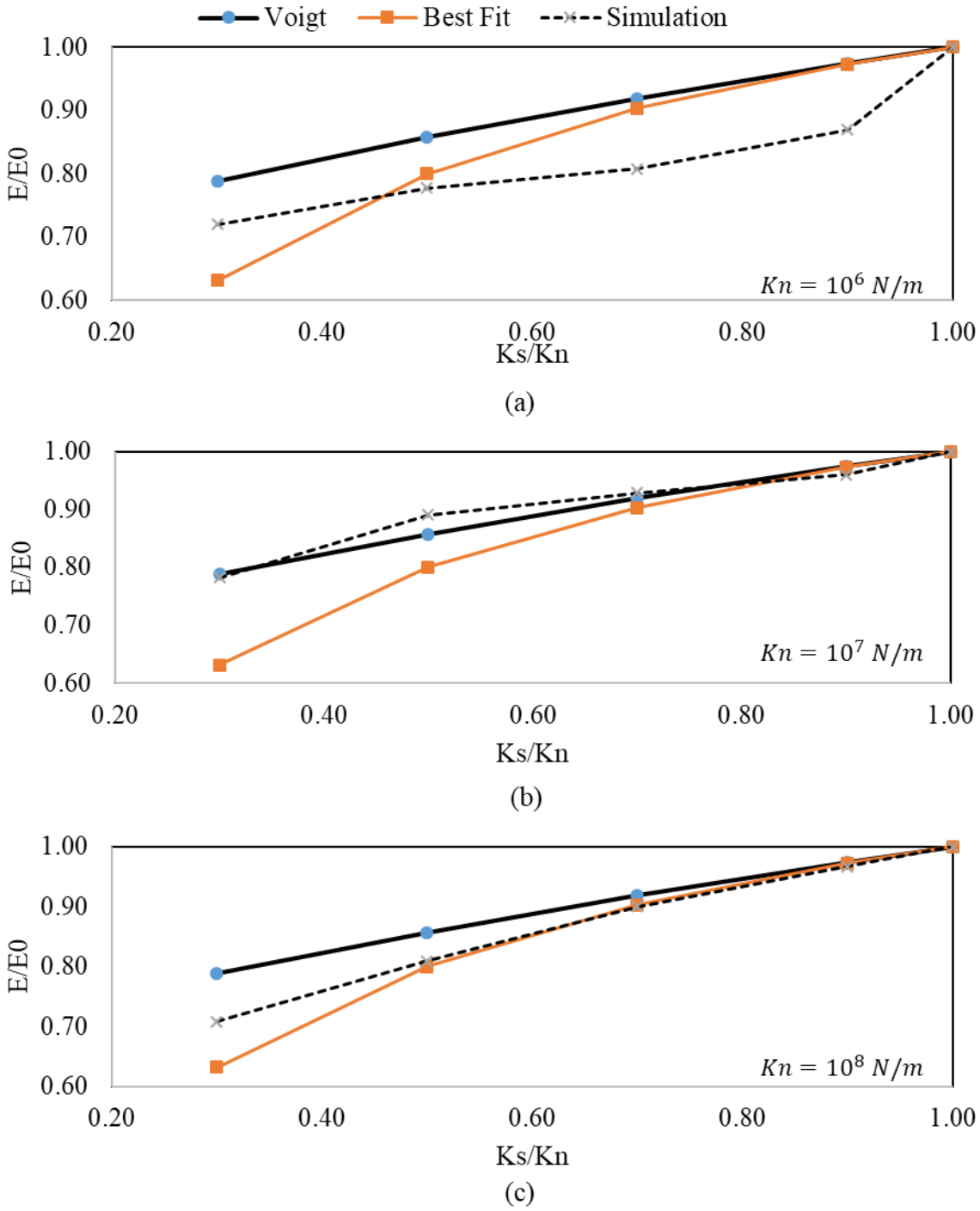

Figure 4.10 Characteristics of Contact Stiffness with Yield Strength (Square Packing)

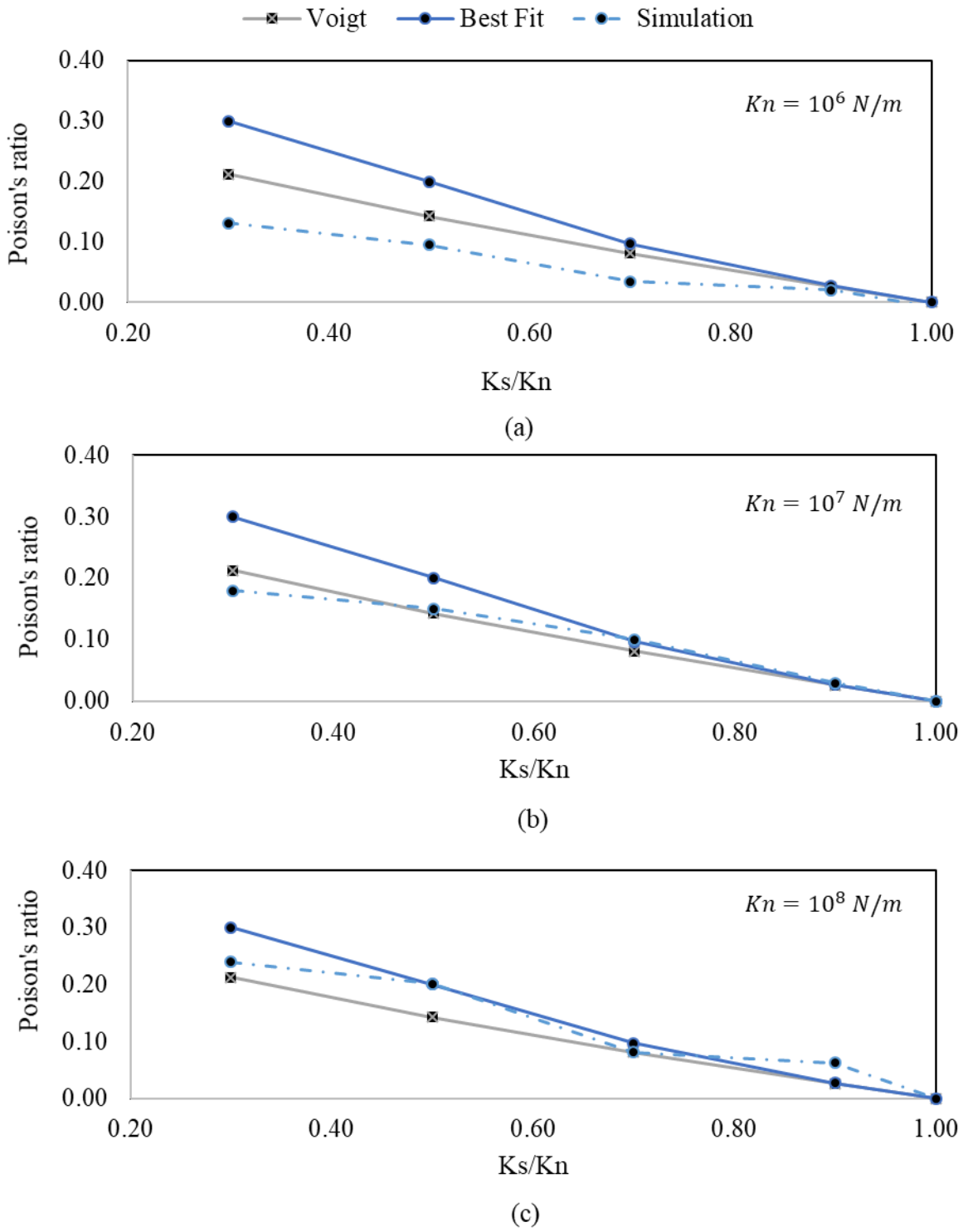

Figure 4.11 Characteristics of Contact Stiffness with Poison's Ratio (Square Packing)

4.8 Comparison of the Results

Wave velocities measured in the simulations differ from the predictions of both the Voigt and Best-Fit theorems. Additionally, triangular packing arrangements exhibit higher wave velocities compared to square packing. Table 4.2 details the percentage difference between the simulation results and the theoretical predictions for both square and triangular packing geometries. Vs is for shear wave velocity, Vp for compressive wave velocity and BF for Best Fit.

Table 4.2 Result Comparison for Shear Wave Velocity

Kn (N/m)	Vs BF(m/s)	Vs Voigt(m/s)	Vs Simulation(m/s)	% difference BF	% difference Voigt
10^6	169	195	161	4.45%	20.81%
	197	209	173	13.90%	20.81%
	219	223	193	13.74%	15.56%
	235	236	208	12.94%	13.10%
	242	242	218	10.74%	10.74%
10^7	533	616	545	-2.22%	13.10%
	624	662	579	7.78%	14.32%
	694	705	610	13.74%	15.56%
	744	745	659	12.94%	13.10%
	765	765	669	14.32%	14.32%
10^8	1685	1949	1759	-4.21%	10.80%
	1974	2094	1864	5.91%	12.34%
	2194	2229	2044	7.34%	9.05%
	2353	2357	2157	9.12%	9.27%
	2418	2418	2268	6.61%	6.61%

Negative percent indicates that the equation result is calculated as less than simulation result. Overall, for shear wave velocity, Best fit solution showing around 8.47% higher velocity than simulation while voigt shows 13.30% more than simulation.

Table 4.3 Result Comparison for Compressive Wave Velocity

Kn (N/m)	Vp BF(m/s)	Vp Voigt(m/s)	Vp Simulation(m/s)	% difference BF	% difference Voigt
10^6	315	322	282	11.76%	14.32%
	322	324	293	10.06%	10.74%
	328	330	295	11.31%	11.91%
	338	338	305	10.67%	10.74%
	342	342	309	10.74%	10.74%
10^7	997	1020	892	11.76%	14.32%
	1019	1026	926	10.06%	10.74%
	1038	1044	933	11.31%	11.91%
	1067	1068	934	14.24%	14.32%
	1081	1081	946	14.32%	14.32%
10^8	3153	3225	2873	9.74%	12.25%
	3224	3244	2984	8.05%	8.72%
	3284	3302	3111	5.57%	6.13%
	3375	3378	3134	7.72%	7.79%
	3419	3419	3207	6.61%	6.61%

Overall, for shear wave velocity, Best fit solution showing around 10.26% higher velocity than simulation while voigt shows 11.04% more than simulation.

Table 4.4 Velocity Difference for Triangular and Square Pattern

Kn (N/m)	Vs Simulation (m/s) Triangular	Vs Simulation (m/s) Square	% difference	Vp Simulation (m/s) Triangular	Vp Simulation (m/s), square	% difference
10^6	161	151	6.89%	282	232	21.71%
	173	159	8.68%	293	238	22.87%
	193	167	15.37%	295	241	22.49%
	208	175	19.30%	305	250	22.16%
	218	190	14.91%	309	268	15.36%
10^7	545	467	16.66%	892	748	19.29%
	579	505	14.74%	926	787	17.75%
	610	527	15.71%	933	791	17.98%
	659	554	18.93%	934	796	17.42%
	669	574	16.59%	946	811	16.59%
10^8	1759	1650	6.61%	2873	2821	1.84%
	1864	1792	4.00%	2984	2929	1.86%
	2044	1992	2.62%	3111	2950	5.44%
	2157	2084	3.50%	3134	3050	2.74%
	2268	2184	3.84%	3207	3088	3.87%

This summarize that both seismic waves increase with respect to normal and shear contact stiffness. P-wave velocity shows a steeper increase with rising contact stiffness in simulations compared to the equation. S-wave velocity exhibits a similar trend, with the simulation results showing a more pronounced rise. Overall good agreement between simulation and equation derived result is obtained and this is more accurate at higher value of Kn. This implies a similar trend observed by (Rojek, Madan, and Nosewicz 2019). To mitigate the deviation between simulated velocities and theoretical predictions, several strategies can be employed. Firstly, as

mentioned, selecting a different contact model can impact the accuracy of simulated results. Each contact model offers distinct assumptions and behaviors. Additionally, altering the method used to determine wave travel time can also reduce errors. While the peak-to-peak method is used in this study, exploring alternative methods such as first arrival, second arrival, and first deflection methods could provide valuable insights and potentially minimize discrepancies.

CHAPTER 5
CONCLUSIONS

5.1 Key Findings

This research investigated the application of the Discrete Element Method to simulate the propagation of seismic waves in granular materials. The study employed a bender element test setup within a DEM model to generate waves and analyze their travel times. The first arrival peak detection method was used to identify wave arrivals at receiver positions.

1. The developed DEM model successfully simulated wave propagation in granular media, allowing for the measurement of S-wave and P-wave velocities. Final result shows, using first peak method, the simulation and equation result yield on average 11% difference between equation and simulation result. This is less then other method described by Lee and Santamarina (2005). Hence first arrival peak detection method proved to be an efficient approach for identifying wave travel times in the DEM simulations.

2. Variations in contact properties (shear and compressive stiffness) within the DEM model significantly impacted the propagation velocities of both S-waves and P-waves. Observed wave velocities were compared with predictions from theoretical models (Voigt and best-fit hypothesis) and showed deviations.

3. The deviations between the DEM simulation results and the predictions from the best-fit hypothesis and Voigt model depends upon the way stress is applied within the simulations. Both theoretical models assume a uniform distribution of stress throughout the simulated domain. In contrast, this study employed gravity as the primary stress source, resulting in a non-uniform stress distribution within the model. This non-uniformity arises because gravity primarily affects the particles near the bottom of the simulation domain, leading to a higher concentration of stress in those regions compared to the top. Since the propagation velocities of seismic waves are

influenced by the material's stiffness and density, which in turn are affected by the stress state, this non-uniform stress distribution in the DEM simulations can lead to deviations in the calculated wave velocities compared to the prediction by equations. Besides, PFC works with the concept of Distinct Element Method while those equations are employed for continuum media leads to the deviations.

5.2 Future Works

1. Future work may involve experimental validation through physical bender element tests on various granular media with different packing densities. By comparing DEM results with measured wave velocities from real materials, the model's accuracy can be assessed, and potential adjustments can be made to mitigate deviations.

2. As highlighted in this study, the current approach using gravity as the primary stress source leads to non-uniform stress distribution. Future work could explore alternative methods for applying stress within the DEM simulations, such as implementing stress confinement conditions on the model boundaries. This could help achieve a more uniform stress state closer to the assumptions of the theoretical models, potentially reducing deviations in wave velocity predictions.

3. The current study employed basic contact models that may not fully capture the intricacies of real-particle interactions. Implementing more sophisticated contact models that account for factors like rolling friction, adhesion, and bonding forces could lead to a more accurate representation of stress distribution and wave propagation.

REFERENCES

Abuawad, Tareq, Gerald Miller, and Kanthasamy Muraleetharan. 2023. “Field and Laboratory Measurements of Shear Wave Velocity in Unsaturated Soils.” Edited by M. Bardanis. *E3S Web of Conferences* 382: 03002. https://doi.org/10.1051/e3sconf/202338203002.

Articolo, George A. 2009. “CHAPTER 5 - The Laplace Partial Differential Equation.” In *Partial Differential Equations & Boundary Value Problems with Maple (Second Edition)*, edited by George A. Articolo, Second Edition, 275–337. Boston: Academic Press. https://doi.org/10.1016/B978-0-12-374732-7.00008-1.

Blewett, J, I J Blewett, and P K Woodward. 2000. “Phase and Amplitude Responses Associated with the Measurement of Shear-Wave Velocity in Sand by Bender Elements.” *Canadian Geotechnical Journal* 37 (6): 1348–57. https://doi.org/10.1139/t00-047.

Cundall, P. A. 1988. “Formulation of a Three-Dimensional Distinct Element Model—Part I. A Scheme to Detect and Represent Contacts in a System Composed of Many Polyhedral Blocks.” *International Journal of Rock Mechanics and Mining Sciences & Geomechanics Abstracts* 25 (3): 107–16. https://doi.org/10.1016/0148-9062(88)92293-0.

Cundall, P. A., and O. D. L. Strack. 1979. “A Discrete Numerical Model for Granular Assemblies.” *Géotechnique* 29 (1): 47–65. https://doi.org/10.1680/geot.1979.29.1.47.

Cundall, Peter A. 1971. “A Computer Model for Simulating Progressive, Large-Scale Movements in Blocky Rock Systems.” In . https://api.semanticscholar.org/CorpusID:131447876.

Dong, Yang, Behzad Fatahi, Hadi Khabbaz, and Henry Zhang. 2018. “Influence of Particle Contact Models on Soil Response of Poorly Graded Sand during Cavity Expansion in

Discrete Element Simulation." *Journal of Rock Mechanics and Geotechnical Engineering* 10 (6): 1154–70. https://doi.org/10.1016/j.jrmge.2018.03.009.

Dyvik, Rune, and Christian Madshus. 1985. "Lab Measurements of G_{max} Using Bender Elements." In , 186–96. ASCE. https://cedb.asce.org/CEDBsearch/record.jsp?dockey=0046357.

Evangelou, Evangelos D., Ioannis N. Markou, Sofia E. Verykaki, and Konstantinos E. Bantralexis. 2023. "Mechanical Behavior of Fiber-Reinforced Soils under Undrained Triaxial Loading Conditions." *Geotechnics* 3 (3): 874–93. https://doi.org/10.3390/geotechnics3030047.

Ferreira, Cristiana, António da Fonseca, and Jaime A. Santos. 2007. "Comparison of Simultaneous Bender Elements and Resonant Column Tests on Porto Residual Soil." In *Soil Stress-Strain Behavior: Measurement, Modeling and Analysis*, edited by Hoe I. Ling, Luigi Callisto, Dov Leshchinsky, and Junichi Koseki, 523–35. Dordrecht: Springer Netherlands.

Hu, Feng, Zhiqing Li, Yifan Tian, and Ruilin Hu. 2021. "Failure Patterns and Morphological Soil–Rock Interface Characteristics of Frozen Soil–Rock Mixtures under Compression and Tension." *Applied Sciences* 11 (1): 461. https://doi.org/10.3390/app11010461.

Jovičić, V., M. R. Coop, and M. Simić. 1996. "Objective Criteria for Determining Gmax from Bender Element Tests." *Géotechnique* 46 (2): 357–62. https://doi.org/10.1680/geot.1996.46.2.357.

Kawaguchi, T, S. Shibuya, and T. Mitachi. 2001. "Evaluation of Shear Wave Travel Time in Laboratory Bender Element Test." *15th Int. Conference on Soil Mechanics and Geotechnical and Engineering*, 155–58.

Lee, Jong-Sub, and J. Carlos Santamarina. 2005. “Bender Elements: Performance and Signal Interpretation.” *Journal of Geotechnical and Geoenvironmental Engineering* 131 (9): 1063–70. https://doi.org/10.1061/(ASCE)1090-0241(2005)131:9(1063).

Liao, Ching-Lung, Ta-Peng Chang, Dong-Hwa Young, and Ching S. Chang. 1997. “Stress-Strain Relationship for Granular Materials Based on the Hypothesis of Best Fit.” *International Journal of Solids and Structures* 34 (31–32): 4087–4100. https://doi.org/10.1016/S0020-7683(97)00015-2.

Mahmood, A. A., and M. Elektorowicz. 2016. “A Review of Discrete Element Method Research on Particulate Systems.” *IOP Conference Series: Materials Science and Engineering* 136 (July): 012034. https://doi.org/10.1088/1757-899X/136/1/012034.

Mas Ivars, Diego, David Potyondy, M Pierce, and PA Cundall. 2008. “The Smooth-Joint Contact Model.” In .

Meegoda, Namunu J., and K. George Chang. 1993. “A NOVEL APPROACH TO DEVELOP A PERFORMANCE BASED TEST FOR RUTTING OF ASPHALT CONCRETE.” In . https://api.semanticscholar.org/CorpusID:106683007.

Mouraille, O., O. Herbst, and S. Luding. 2009. “Sound Propagation in Isotropically and Uni-Axially Compressed Cohesive, Frictional Granular Solids.” *Engineering Fracture Mechanics* 76 (6): 781–92. https://doi.org/10.1016/j.engfracmech.2008.09.001.

O’Donovan, J., C. O’Sullivan, and G. Marketos. 2012. “Two-Dimensional Discrete Element Modelling of Bender Element Tests on an Idealised Granular Material.” *Granular Matter* 14 (6): 733–47. https://doi.org/10.1007/s10035-012-0373-9.

Pennington, DS, DFT Nash, and ML Lings. 2001. “Horizontally Mounted Bender Elements for Measuring Anisotropic Shear Moduli in Triaxial Clay Specimens.” *Geotechnical Testing Journal* 24 (2): 133–44. https://doi.org/10.1520/GTJ11333J.

“PFC — PFC 6.0 Documentation.”. Accessed March 6, 2024. https://docs.itascacg.com/pfc600/pfc/docproject/source/manual/pfc_model_components/pfc_model_components.html?node1197.

Rojek, Jerzy, Carlos Labra, Okan Su, and Eugenio Oñate. 2012. “Comparative Study of Different Discrete Element Models and Evaluation of Equivalent Micromechanical Parameters.” *International Journal of Solids and Structures* 49 (13): 1497–1517. https://doi.org/10.1016/j.ijsolstr.2012.02.032.

Rojek, Jerzy, Nikhil Madan, and Szymon Nosewicz. 2019. “Micro–Macro Relationships in the Simulation of Wave Propagation Phenomenon Using the Discrete Element Method.” *Materials* 12 (24): 4241. https://doi.org/10.3390/ma12244241.

Sadd, Martin H., Qiming Tai, and Arun Shukla. 1993. “Contact Law Effects on Wave Propagation in Particulate Materials Using Distinct Element Modeling.” *International Journal of Non-Linear Mechanics* 28 (2): 251–65. https://doi.org/10.1016/0020-7462(93)90061-O.

Shirley, Donald J, and Loyd D Hampton. 1978. “Shear-Wave Measurements in Laboratory Sediments.” *J. Acoust. Soc. Am.* 63 (2): 7.

Thornton, C. 2000. “Numerical Simulations of Deviatoric Shear Deformation of Granular Media.” *Géotechnique* 50 (1): 43–53. https://doi.org/10.1680/geot.2000.50.1.43.

Viggiani, Giulia, and J. H. Atkinson. 1995. “Interpretation of Bender Element Tests.” *Géotechnique* 45 (1): 149–54. https://doi.org/10.1680/geot.1995.45.1.149.

Yin, Peng-Fei, and Sheng-Qi Yang. 2019. “Discrete Element Modeling of Strength and Failure Behavior of Transversely Isotropic Rock under Uniaxial Compression.” *Journal of the Geological Society of India* 93 (2): 235–46. https://doi.org/10.1007/s12594-019-1158-0.